Isotopic insights into the sources and turnover of organic carbon and methane in fjord and shelf sediments off northern Norway

Simone Sauer[a,b,], Wei Li Hong[b], Jochen Knies[a,b], Aivo Lepland[a,b], Matthias Forwick[c], Martin Klug[a], Florian Eichinger[d], Soma Baranwal[b], Antoine Crémière[a,b], Shyam Chand[a,b], Carsten J. Schubert[e]*

Accepted at G-cubed with moderate revision

[a] Geological Survey of Norway, Trondheim, Norway

[b] CAGE – Centre for Arctic Gas Hydrate, Environment and Climate, Department of Geology, UiT the Arctic University of Norway, 9037 Tromsø, Norway

[c] Department of Geology, UiT the Arctic University of Norway, 9037 Tromsø, Norway

[d] Hydroisotop GmbH, Schweitenkirchen, Germany

[e] Eawag, Swiss Federal Institute of Aquatic Science and Technology, Kastanienbaum, Switzerland

* Corresponding author. Tel.: +47 73904169; *Email address*: simone.sauer@ngu.no

Key points:

- Comparison of carbon cycle between shelf and fjord settings in northern Norway
- Carbon source for biogeochemical reactions is supplied by marine organic matter in the fjord and by thermogenic CH4 seepage on the shelf
- In spite of similar sulphate pore water profiles organoclastic sulphate reduction is higher in the fjord and AOM is higher on the shelf

Abstract

To better understand the present and past carbon cycling and transformation processes in methane influenced fjord and shelf areas we compared two sediment cores from the Hola trough and from Ullsfjorden, northern Norway.

We investigated (1) the organic sediment composition and sedimentological characteristics to study the sources of organic carbon (C_{org}) and the factors influencing C_{org} burial, (2) pore water geochemistry to determine the different organic matter degradation processes, and (3) the carbon isotopic signatures of hydrocarbon to identify the carbon transformation processes and gas sources.

The notion that fjords are important C_{org} sinks is supported by the sediment core from Ullsfjorden showing high sedimentation and C_{org} accumulation rates during the Holocene. The depth of the sulphate-methane-transition (SMT) is controlled by the supply of marine organic matter to the sediment. Sulphate reduction coupled to organic matter degradation accounts for 60% of the total depth-integrated sulphate reduction in the fjord. In spite of the presence of ethane, propane and butane, we suggest a purely microbial origin of light hydrocarbons in the sediments based on their light $\delta^{13}C$ values.

In the Hola trough, sedimentation and C_{org} accumulation rates changed during the deglacial-to-post-glacial transition from approximately 80 cm ka^{-1} to erosion at present. Thus, burial of organic matter on this part of the shelf is presently absent. Low organic matter content in the sediment and low rates of sulphate reduction coupled to organic matter degradation (only 3% of total sulphate reduction) entail that the shallow SMT is controlled mostly by ascending thermogenic methane from deeper sources.

1 Introduction

Continental shelves and fjords play an important role in the global carbon cycle. However, due to variable primary productivity, sedimentation and early diagenetic regimes, uncertainties in estimates of carbon fluxes for these areas remain. There is currently no consensus on the exact role of shelves and fjords in the carbon cycle, which complicates the quantification of sinks and sources and hinders the integration in global carbon cycle models (Bauer et al., 2013; Keil, 2015; Smith et al., 2015). Shelf areas occupy only 7-10% of the global ocean area but contribute 10-30% to the global marine primary production (Wollast, 1991; Bauer et al., 2013) and are, therefore, important areas of organic carbon (C_{org}) production. Thus, shelves are also assumed to be important areas for carbon burial (Berner, 1982; Hedges and Keil, 1995), with a majority (>80%) of C_{org} burial in deltaic-shelf sediments near river mouths (Berner, 1982). Furthermore, CO_2 air-sea exchange studies suggest that most shelves are a net sink for atmospheric CO_2 (Cai et al., 2006; Laruelle et al., 2010; Chen et al., 2013).

A recent study by Smith et al. (2015) highlights the importance of fjords in C_{org} burial, estimating that 11% of annual marine carbon burial takes place in fjords although they account for only <0.1% of the marine surface area (Keil, 2015). Due to a much larger area occupied by shelves than fjords, shelves still play a bigger role in total C_{org} burial (129 gC yr^{-1}) than fjords (18 gC yr^{-1}), but area-normalized burial rates are more than five times higher in fjords (Smith et al., 2015). Fjords are such "hot spots" of carbon burial because they are much deeper than the adjacent sea which causes effective trapping and rapid accumulation of sediments (Keil, 2015).

There are several factors controlling the burial and preservation of organic carbon (C_{org}) such as primary productivity, sediment accumulation rate, bottom water oxygenation and organic matter source (Hedges and Keil, 1995). High primary productivity can increase C_{org} burial due to a higher flux of C_{org} through the water column. A higher sedimentation rate enhances C_{org} burial (Müller and Suess, 1979) due to reduced exposure time at the sediment-water interface where early diagenetic decomposition is most effective. Early diagenetic decomposition is further reduced by low bottom

water oxygen concentrations which exerts a control on C_{org} preservation (Hartnett et al., 1998). Furthermore, marine organic matter (MOM) such as fresh algal detritus is easier degradable, than for example land-derived macromolecules like lignin, and thus less likely to be preserved (Henrichs, 1992).

Information about early diagenetic processes influencing C_{org} degradation, burial, rates of methanogenesis and methane oxidation can be deduced from pore water geochemical profiles and inferred redox boundaries in the sediment (Sommer et al., 2006; Boetius and Wenzhöfer, 2013; Hong et al., 2014b; Hong et al., 2016 accepted). One of the most prominent features in sediment pore water profiles is the sulphate-methane transition zone (SMT) where sulphate reduction and the anaerobic oxidation of methane (AOM) are performed by a consortium of sulphate-reducing bacteria and anaerobic methanotrophic archaea (e.g. Hinrichs et al., 1999; Boetius et al., 2000). Anaerobic oxidation of methane is the main microbial process preventing methane produced in marine sediments from reaching the seafloor (e.g. Reeburgh, 2007; Pohlman et al., 2013). In most settings the depth of the SMT is determined by (1) the amount and quality of organic matter buried which influences sulphate consumption by organoclastic sulphate reduction (e.g. Borowski et al., 1999) and (2) by the methane flux from below (e.g. Borowski et al., 1996).

To better understand the present and past carbon cycling and transformation processes in methane influenced fjord and shelf areas we compared two sediment cores from the continental shelf offshore the Vesterålen Islands (Hola trough) and from Ullsfjorden, northern Norway. To assess C_{org} burial and sources we analysed the concentration of organic matter and its isotopic composition. We conducted radiocarbon (AMS-^{14}C) dating and analyses of sediment physical properties such as grain size, magnetic susceptibility and bulk density to reconstruct sedimentation history and accumulation rates. Furthermore, we used sediment pore water profiles to deduce early diagenetic processes and to perform transport reaction modelling to quantify organic matter degradation rates by sulphate reduction and methanogenesis and to determine AOM rates and factors controlling SMT depth in the shelf and the fjord setting. Moreover, we applied stable carbon and hydrogen isotope analyses on

the gases from the sediment below the SMT to define the source of gas (e.g. Whiticar, 1999) and investigate the possible transformation processes of carbon in the sediment. We used $\delta^{13}C$ and $\delta^{2}H$ of methane, $\delta^{13}C$ of dissolved inorganic carbon (DIC) and also $\delta^{13}C$ of ethane and propane to assess microbial and thermogenic contribution of gases (Whiticar et al., 1986; Chung et al., 1988; Whiticar, 1999; Katz et al., 2002; Hinrichs et al., 2006; Vandré et al., 2007), possible hydrocarbon biodegradation (Jones et al., 2008; Etiope et al., 2009; Katz, 2011; Milkov, 2011) and different methanogenic pathways (Botz et al., 1996; Conrad, 2005; Heuer et al., 2009). Moreover, we evaluated the results of C_{org} source and content in the context of sedimentation dynamics and rates of early diagenetic reactions and assessed C_{org} deposition, C_{org} burial and/or degradation, transformation via methanogenesis and AOM in order to contribute to the understanding of the organic carbon cycle in shelf and fjord environments.

2 Study areas

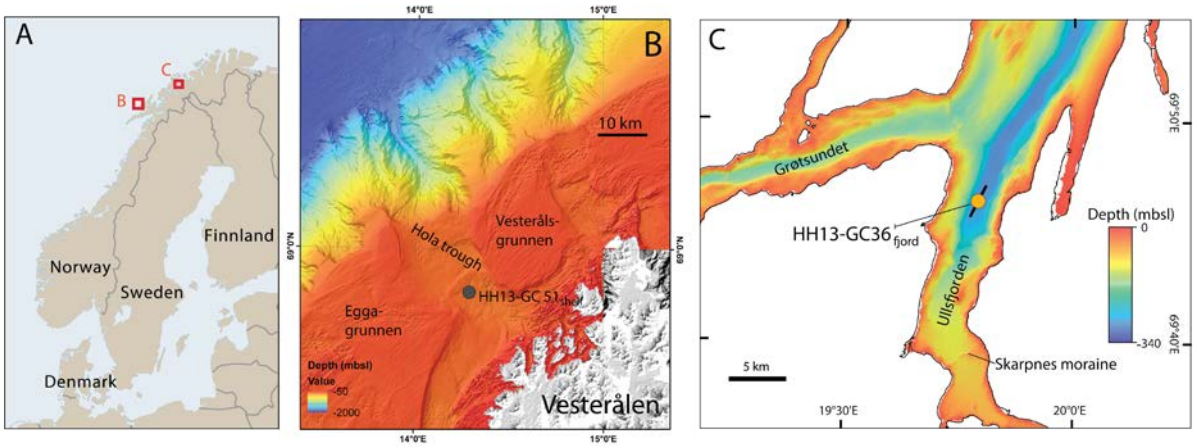

Figure 1: Map of Scandinavia (A), the Vesterålen shelf with the Hola trough and location of gravity core HH13 - GC 51$_{shelf}$ (B) and Ullsfjorden with the location of gravity core HH13 - GC 36$_{fjord}$ and the chirp line (black line) (C).

2.1 Vesterålen shelf/ Hola trough

The continental shelf offshore the Vesterålen Islands (Figure 1), northern Norway, is relatively narrow and characterized by alternating shallow banks and deeper troughs which were formed during the last glaciations (Bøe et al., 2009). The Hola trough, is a cross shelf trough, which is ca. 12 km wide with water depths of around 200 m and high bottom current speeds. The Hola trough is

confined by the banks Vesterålsgrunnen to the NE and Eggagrunnen to the SW (Figure 1B). The Norwegian Atlantic Current flows northward over the upper slope and causes sediment winnowing down to at least 500 m forming sand and gravel lag deposits, also found in the Hola trough (Elvsborg, 1979; Bøe et al., 2009). Active methane seeps from certain areas of the Hola trough were discovered in 2008 (Chand et al., 2008) and further investigated by Sauer et al. (2015) who found that the hydrocarbon gas is predominantly of thermogenic origin most likely derived from Late Jurassic to Early Cretaceous source rocks in the region.

2.2 Ullsfjorden

Ullsfjorden is a north-south oriented fjord in Troms County, northern Norway (Figure 1C). The fjord is ca. 70 km long with a maximum water depth of 285 m (Plassen and Vorren, 2003b). The sediment in the fjord is largely composed of glaciomarine trough fill with thicknesses up to 200 m deposited during deglaciation (Vorren et al., 1989). Ullsfjorden was deglaciated between about 15-11 cal ka BP (Plassen and Vorren, 2003a). The Skarpnes moraine (Figure 1C), about 13 km south of the study area was dated to 14-13.9 cal ka BP (Plassen and Vorren, 2003a) and sediment deposition in an open marine environment started around 11 cal ka BP (Plassen and Vorren, 2003b). The post-glacial sediment thickness in our study area is around 15 m (Figure 2).The bottom of Ullsfjorden is characterized by ubiquitous pockmarks (Plassen and Vorren, 2003b), suggested to have been formed as a result of gas escape or groundwater-related processes (Hovland and Judd, 1988; Plassen and Vorren, 2003b).

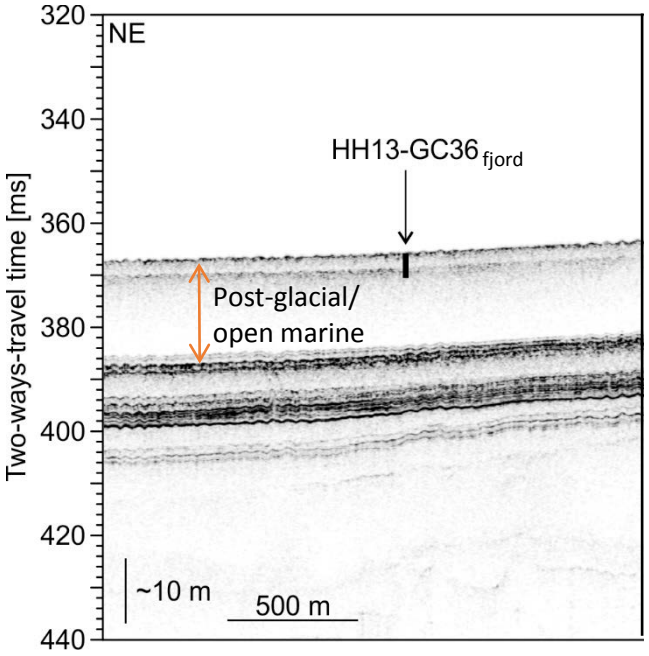

Figure 2: Chirp profile crossing the location of core HH13-GC 36$_{fjord}$ (for location see Fig. 1C).

3 Material and methods

We collected two gravity cores HH13-GC 51$_{shelf}$ and HH13-GC 36$_{fjord}$ (hereafter referred to as GC 51$_{shelf}$ and GC 36$_{fjord}$) during RV Helmer Hansen cruise in April 2013. GC 51$_{shelf}$ was retrieved from the continental shelf offshore Vesterålen at a water depth of 222 m and GC 36$_{fjord}$ was taken from Ullsfjorden at a water depth of 276 m (Table 1 and Figure 1).

Table 1: Location, water depth at sampling site and the recovered length of the two gravity cores GC 36$_{fjord}$ and GC 51$_{shelf}$.

Station name	Latitude (N)	Longitude (E)	Water depth (m)	Coring device	Recovery (cm)
GC 36$_{fjord}$	69.7852	19.8096	276	gravity corer	380
GC 51$_{shelf}$	68.9179	14.2858	222	gravity corer	312

3.1 Sampling

Immediately after core retrieval we sampled the cores for gas using headspace vials prefilled with 6 ml NaOH (2.5%), and pore water using the rhizone technique (Seeberg-Elverfeldt et al., 2005) in intervals of 25 cm (for details see Sauer et al., 2015). The gravity cores were subsequently cut into 1 m sections and stored frozen.

After thawing the cores, the 1 m sections were split in 2 halves (archive and working half) using a

core splitter at the Geological Survey of Norway (NGU). Sediment samples of ca. 10 ml sediment were collected from the working halves in 5 cm intervals for the determination of elemental composition, grain size distribution, carbon and nitrogen content, as well as $\delta^{13}C$-C_{org}. All samples (except those for grain size analyses) were freeze dried and homogenized using a Fritsch Micro Mill PULVERISETTE 7 with agate grinding bowls and balls.

3.2 Pore water analyses

Dissolved phosphate (PO_4^{3-}) was determined photometrically with a Shimadzu UVmini-1240 UV-Vis Spectrophotometer using the method after Murphy and Riley (1962) on board RV Helmer Hansen.

Dissolved sulphide was measured by the photometric methylene blue method (Cline, 1969) on a DR5000 UV-VIS Spectrophotometer at the University of Bremen, Germany. NH_4^+ was detected with a flow injection teflon tape gas separator technique after Hall and Aller (1992) at the University of Bremen. The anion sulphate (SO_4^{2-}) was determined using a Dionex ICS - 1100 Ion Chromatograph with a Dionex AS-DV autosampler and a Dionex IonPac AS23 column at the NGU (relative standard deviation: ± 0.7%, 1σ, n = 10, standard: SPEX CertiPrep). Methane concentration dissolved in the sediment pore water was analysed by equilibrium partitioning and measured at the Swiss Federal Institute of Aquatic Science and Technology (EAWAG) using an Agilent Gas Chromatograph G1530N with a flame ionization detector (standard deviation ± 2.9%). For CH_4 concentration in the pore water the calculated CH_4 concentration per sediment volume was corrected with an assumed constant sediment porosity of 0.8 (Haeckel et al., 2001).

The stable carbon isotopes of methane (C_1), ethane (C_2), propane (C_3), *i*-butane (*i*-C_4) and *n*-butane (*n*-C_4) and hydrogen isotopes of methane were analysed at Hydroisotop GmbH, Germany, with a GC-MS-IRMS system (Thermo Fischer Scientific GmbH). The isotopic composition is reported in ‰ (δ-values) against the international standards Vienna Pee Dee Belemnite (VPDB) for $\delta^{13}C$ and Vienna Standard Mean Ocean Water (VSMOW) for $\delta^{2}H$. Methane carbon isotope composition ($\delta^{13}C$-CH_4) was also determined with a trace gas analyser connected to a mass spectrometer (GV Instruments) at

EAWAG.

The stable carbon isotopes of dissolved inorganic carbon (δ^{13}C-DIC) in the pore water samples were determined with a gas bench coupled to a Delta V Plus mass spectrometer (Thermo, Switzerland) at ETH Zürich and at EAWAG using a multiflow connected to an Isoprime mass spectrometer (GV Instruments, UK). More details of the individual analyses are described in Sauer et al. (2015).

3.3 Geochemical analyses

Analyses of total carbon (TC) and C_{org} were performed with a LECO SC-632 at the Laboratory of NGU. For TC determination 300-400 mg of subsample were combusted at 1350°C and the production of CO_2 determined. For C_{org} analysis 400-450 mg of subsamples were placed in carbon-free pervious ceramic combustion boats. These were placed on a heating plate with 50°C (± 5°C) and samples were treated with 10 vol.% hydrochloric acid (HCl) to remove inorganic carbon (carbonate) and subsequently rinsed with distilled water and dried in the drying oven prior to analysis. Results are given in weight percentage (wt%) and the standard deviation of the TC and C_{org} measurements based on the repeated measurement of a standard was ± 0.026 wt% (1σ, n=8) and ± 0.028 wt% (1σ, n=11), respectively.

Total nitrogen (N_{tot}) was analysed with a LECO FP 628 Nitrogen determinator at NGU. A subsample of 200 mg was placed in tin foil and combusted to NO_x which was transformed to N_2 and detected with a thermal conductivity cell. The standard deviation of the N_{tot} measurements based on the repeated measurement of a nitrogen standard was ± 0.01 wt% (1σ, n=11). The C/N ratio was calculated by dividing the C_{org} content (wt%) by the nitrogen content (wt%) and multiplying with 1.167 to obtain the atomic relationship.

3.4 Isotopic analyses and radiocarbon dates

δ^{13}C of C_{org} was analysed by EA-IRMS (Elemental Analyser Isotope Ratio Mass Spectrometry) at Iso Analytical Ltd, UK. Subsamples were decarbonated with 10 vol% HCl prior to analysis with a RoboPrep-CN elemental analyser coupled to a Europa Scientific 20-20 IRMS. Sample duplicates and

reference materials were analysed for quality control. The standard deviation (based on the reference material measurements) was ±0.06‰.

^{14}C analyses were carried out by accelerator mass spectrometry (AMS) at the 14Chrono Centre at the Queens University, Belfast, with a NEC compact model 0.5 MV AMS. Samples for ^{14}C analysis (foraminifera and shell fragments) were pre-treated in an ultrasonic bath to remove dirt and etched with 1% HCl. Subsequently, they were hydrolyzed to CO_2 using dehydrated 100% orthophosphoric acid before isotopic analysis. The calibration of ^{14}C ages was performed with clam 2.2 (Blaauw, 2010) using the Marine13 calibration curve (Reimer et al., 2013) and ages are reported in calibrated calendar years before present (cal yr BP; present = 1950).

3.5 Sedimentological analyses

Whole core measurements, i.e. wet bulk density (WBD) and magnetic susceptibility (MS) were conducted on the frozen gravity cores using the Standard MSCL-S core logger (GeoTek Ltd., UK) at 0.5 cm resolution with 5 sec measurement time. Dry bulk density (DBD) was calculated from the WBD density following the procedure described by Weber et al. (1997). C_{org} accumulation rates were calculated from linear sedimentation rates (based on the calibrated ages) and averages of DBD and C_{org} content of the sediment between each pair of ages.

MS measurements for whole cores were done with a Bartington MS2C loop sensor (Dearing, 1994) with 130 mm coil diameter. The MS2C loop sensor measurement represents data integrated over a distance equivalent to the sensor diameter which is symmetrically located before and behind the sensor along the core axis (Nowaczyk, 2002). For control of the MS2C sensor, a certified sample piece with known magnetic susceptibility was measured. The raw magnetic susceptibility data is processed to corrected volume specific magnetic susceptibility, which takes into account the relative effect of size of the core and the size of the loop sensor being used.

After lengthwise splitting and surface cleaning core surface images were taken with the GeoScan colour line-scan camera. The camera was equipped with a AF Nikkor 50mm f/1.8D lens and three

detectors using three 2048 pixel charge-coupled device CCD arrays for red, green and blue light. The core surface was continuously imaged with 100 µm down and cross core resolution. Each core section was measured with an X-rite ColorChecker as reference for basic color control.

X-ray images (XRI) of split cores were taken with the Geotek MSCL-XCT (Geotek Ltd., UK). The Geotek MSCL-XCT is equipped with a Thermo Kevex PSX10-65W X-ray source (Thermo Fisher Scientific Inc., USA) and a Varian PAXScan 2520V (Varian Medical Systems, Inc., USA) with a 1920 x 1536 pixel array as X-ray detector. The micro-focal X-ray source was used with a voltage of 87 and 120 kV and a current of 125 and 140 µA for cores GC 36_{fjord} and GC 51_{shelf}, respectively. The 1x1 0.5pF G4 10 fps detector-CCD-mode was used for highest resolution.

The grain size distribution (0.4 µm – 2000 µm) was determined using a Coulter LS 200. To prevent charging and agglomeration of particles, samples were treated with 5 % sodium pyrophosphate ($Na_4P_4O_7$ x $10H_2O$, MerckPA) and sonicated. Grain sizes above 2000 µm were determined by dry sieving. A duplicate of each sample was analysed and the relative error was ±10%.

3.6 Chirp

High-resolution seismic ("chirp"-) data were collected with a hull-mounted Edgetech 3300-HM sub-bottom profiler (4*4 arrays). The pulse mode was 1.5-9.0 kHz, 40 ms pulse length, and a shot rate of 1 Hz.

3.7 Pore water modelling

We use CrunchFlow, a FORTRAN-based routine designed to simulate solute diffusion and biogeochemical reactions (Steefel, 2009), to investigate and quantify the biogeochemical reactions. CrunchFlow has been applied in various cases to study the biogeochemical processes and fluid flow in ground water, geological reservoirs, and marine sediments (Hong et al., 2014a; Steefel et al., 2014; Steefel et al., 2015; Zhang et al., 2015; Hong et al., 2016 accepted). We simulated both the concentrations of solutes in pore water and the carbon isotopes of DIC and methane. We included no advection component in our modelling as the pore water profiles show no sign of fluid advection. We

ran the simulation for 4.04 ka and 18 ka for station GC 36_{fjord} and GC 51_{shelf}, respectively, according to ages determined for the base of the cores (^{14}C dating section). Such length of time is sufficient for the pore water system to reach steady state. We included the following biogeochemical reactions in the model: particulate organic carbon sulphate reduction (POCSR), methanogenesis (ME), anaerobic oxidation of methane (AOM) secondary CO_2 reduction (CR). The detailed mathematical formulation of all these reactions and essential parameters are summarized in the supplementary materials.

4 Results

4.1 Sedimentology

The x-ray images and colour photos as well as the physical properties such as WBD and MS of core GC 36_{fjord} and GC 51_{shelf} are presented in Figure 3.

The sediment colour of core GC 51_{shelf} varies between dark grey (2.5Y 4/1) and very dark grey (2.5Y 3/1). Three lighter intervals occur between 40-44 cm, 20-26 cm and 0-4 cm. The lowermost 20 cm of the core are coarse grained with on average 26% of the >63 µm fraction (sand and coarser). A marked fining occurs around 290 cm with increases in the clay and silt fraction (Figure 3). Between 290 cm and 170 cm the grain size distribution is relatively constant (13.5% clay, 80% silt, and 6.5% sand and coarser). A gradual coarsening occurs in the uppermost ca. 170 cm. Silt content decreases from 80% at 170 cm to 7% at 1 cm depth, whereas the >63 µm fraction increases from 8% to 91% in the same interval. In accordance with grain size, MS is highest at the top of the core. Below 100 cm MS is on average 30 *10-5 SI (Figure 3). Between 100 and 10 cm depth MS is on average 60 *10-5 SI and at 2 cm sediment depth magnetic susceptibility values reach up to 1200 *10-5 SI. The WBD below 290 cm is approximately 2 g cm^{-3}. At 290 cm, there is a density drop to 1.5 g cm^{-3} coinciding with the marked fining of the sediment. The density increases gradually from ca. 1.5 g cm^{-3} at 290 cm to 2 g cm^{-3} at the top of the core. The x-ray images of core GC 51_{shelf} reveal that the lowermost 10 cm of the core contain several larger clasts and that there is strong lamination from 200 cm to 80 cm.

The sediment colour of core GC 36$_{fjord}$ varies between olive (5Y 4/4) and olive grey (5Y 4/2). The grain size distribution is constant throughout the core with a silt content of 89% and on average 6% of the <63 µm fraction. The only exception is one interval at 137-140 cm depth where silt content decreases to 77 % and an increase in the >63 µm fraction up to 19% can be observed (Figure 3). Magnetic susceptibility is lower throughout GC 36$_{fjord}$ (average is 13 *10-5 SI) compared to GC 51$_{shelf}$. WBD is on average 1.46 g cm^{-3} in the lowermost 250 cm of the core and decreases down to 1 g cm^{-3} towards the top of the core in the uppermost 130 cm. Only the interval with coarser grain sizes has a higher density of 1.6 g cm^{-3} (Figure 3). The x-ray imaging shows a homogenous core without any lamination. The only feature is a darker shade of the coarser, denser interval at 137-140 cm.

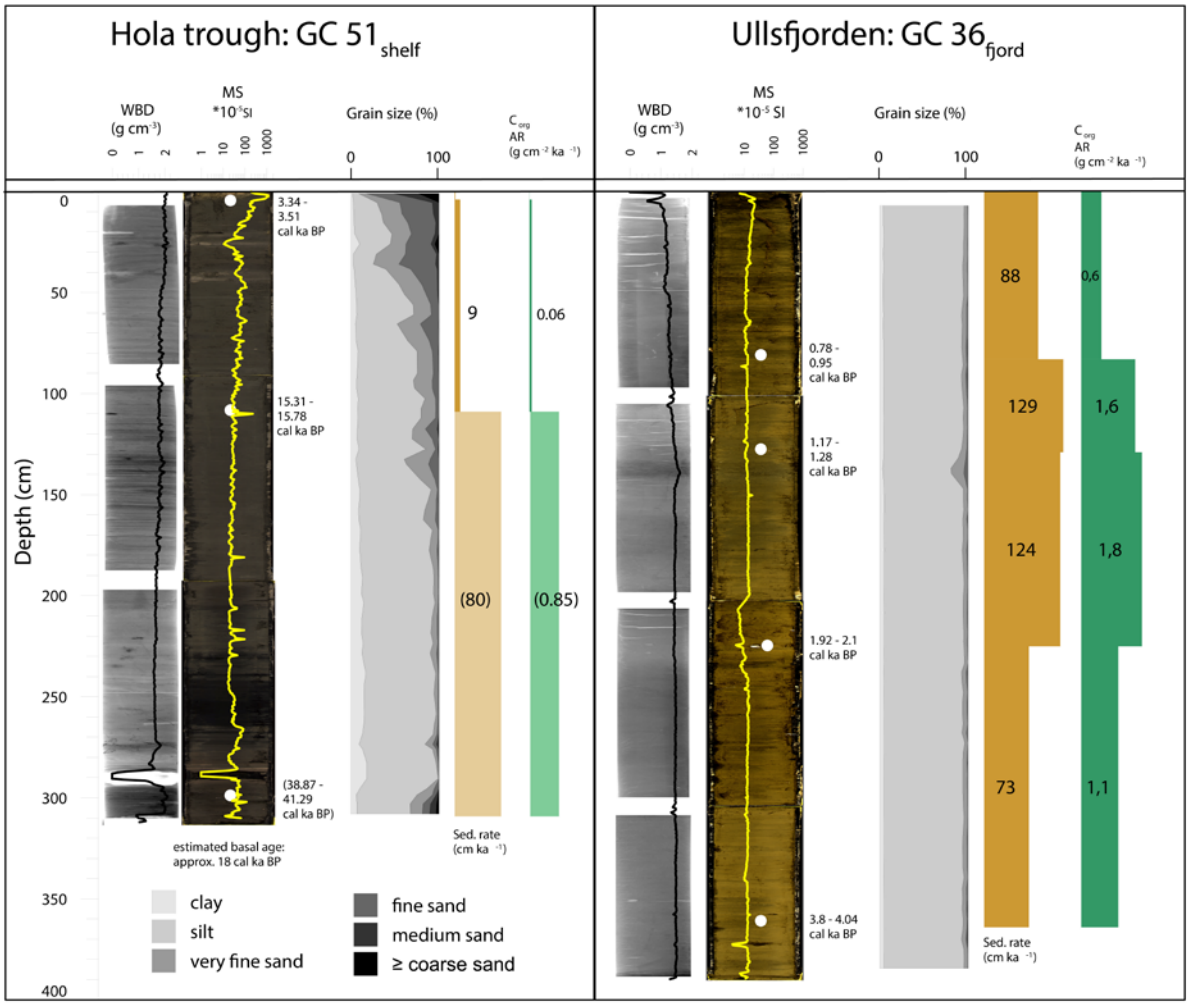

Figure 3: Sedimentological characteristics of cores GC 51$_{shelf}$ and GC 36$_{fjord}$: XRI and colour photos (stretched horizontally 400%), density (black line on top of X-ray image), magnetic susceptibility (yellow line on top of colour photo), calibrated ages, grain size distribution, sedimentation rate and C_{org} accumulation rate. Notice the lighter shading of the sedimentation rate and C_{org} accumulation rate below 110 cm in GC 51 indicating the uncertainty in these estimates due to the uncertain basal age.

4.2 Chronology and sedimentation rates

Table 2: Results of AMS ^{14}C dating of different carbonate materials (foraminifera and shells) from core GC 36_{fjord} and GC 51_{shelf}.

					calibrated years BP (2σ)	
Core	*Depth*	*Lab ID*	*Material*	*^{14}C age BP*	*maximum*	*minimum*
GC 36_{fjord}	82-83 cm	UBA-25349	*Thyasira granulosa*	1,333±34	948	784
	128-129 cm	UBA-25350	*Musculus niger*	1,665±26	1,282	1,170
	224-225 cm	UBA-25351	*Thyasira granulosa*	2,377±28	2,101	1,916
	363-364 cm	UBA-25352	*Thyasira granulosa*	3,920±37	4,044	3,802
GC 51_{shelf}	3-4 cm	UBA-21635	Mixed benthic and planktic foraminifera	3,537±30	3,513	3,344
	108-109 cm	UBA-21636	shell fragment	13,406±59	15,780	15,310
	299.5-300.5 cm	UBA-21637	Mixed benthic and planktic foraminifera	35,865±596	41,290	38,870

We obtained three ^{14}C ages from core GC 51_{shelf} and four from GC 36_{fjord} (Table 2). In core GC 36_{fjord} we expect the top of the core to represent present sedimentation. The sample closest to the bottom of the core was dated to between 3,802-4,044 cal years BP. The uppermost sample of core GC 51_{shelf} (3-4 cm) gave an age between 3,344-3,513 cal years BP. The sample at 300 cm sediment depth, consisting of a mix of benthic and planktic foraminifera, was dated to between 38,870-41,290 cal years BP with an error of ±596 years. We suspect this is due to re-deposition of foraminifera from older strata not representing the actual age of the sediment in this depth interval.

Average sedimentation rates calculated between each pair of ^{14}C dates vary between 73-129 cm ka^{-1} in core GC 36_{fjord} (Figure 3). For core GC 51_{shelf}, the sedimentation rate between the upper two ^{14}C dates was 9 cm ka^{-1}, which is around 10 times lower than that in core GC 36_{fjord}. We disregarded the lowest ^{14}C age in core GC 51_{shelf} and instead estimated the bottom age to 18 cal ka BP based on the sedimentology of the core which suggests that the lowermost part is a basal till/glacimarine diamicton deposited between 17.5 and 18 cal ka BP according to the reconstruction of glacier retreat by Vorren et al. (2015). The interpretation is based on the high abundance of angular large clasts, high density and the absence of layering in the lower 5 cm of the core (Forwick and Vorren, 2009).

The resulting average sedimentation rate is then 80 cm ka^{-1} for the lowermost 2 m of core GC 51_{shelf} (Figure 3).

4.3 Organic sediment geochemistry

The C_{org} content in the lowermost 10 cm of GC 51_{shelf} is around 0.6% (Figure 4). A peak up to 1.9% C_{org} at 282 cm is observed and a steady decrease from 1% at 270 cm to 0.2% at 5 cm depth. The total nitrogen content (N_{tot}) of the sediment decreases slightly upwards through the core from 0.09% to 0.03% (average: 0.06%, n= 62). The C/N ratio shows a peak at 288 cm of 31, coinciding with the peak in C_{org}. From 270 cm to the top of the core the C/N ratio decreases from ~18 to ~9. The average C/N ratio of core GC 51_{shelf} is 14.8 ± 3.3. The average $\delta^{13}C$-C_{org} of core GC 51_{shelf} is -24.8‰ (±0.47‰, n=62). In the interval between 288 cm and 283 cm $\delta^{13}C$-C_{org} is heavier (around -23.9‰) and between 45 cm and 35 cm $\delta^{13}C$-C_{org} is lighter (around -26‰) than the average.

C_{org} content is 1.8% at the bottom of core GC 36_{fjord} and increases steadily to 2.9% at 5 cm depth, interrupted by a sharp drop to 1.4% at 141 cm depth (Figure 4, blue band).The N_{tot} content increases gradually from 0.27% at the bottom of the core to 0.4 % at 5 cm depth with one negative excursion to 0.2% at 140 cm depth, showing the same pattern as the C_{org} content. The atomic C/N ratio is constant throughout the core with an average of 7.7 ± 0.2. The $\delta^{13}C$-C_{org} values also show little variation throughout the core with an average of -21.04‰ ± 0.14‰.

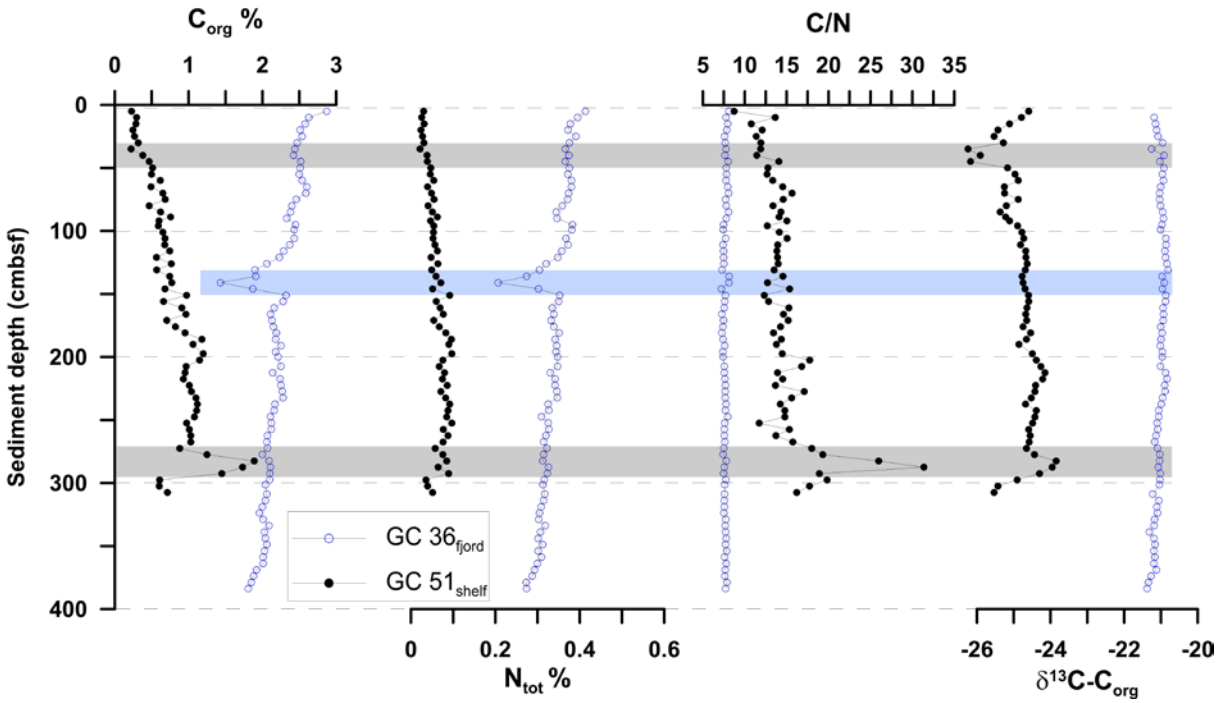

Figure 4: Concentrations of C_{org}, total nitrogen (N_{tot}), C/N ratio and $\delta^{13}C$-C_{org} of sediment core GC 36_{fjord} (blue empty circles) and GC 51_{shelf} (black filled circles). The grey shaded areas mark intervals of core GC 51_{shelf} where pronounced changes in $\delta^{13}C$-C_{org} and/or C/N ratio are observed. The blue shaded area marks an interval of re-deposited sediment in GC 36_{fjord}.

4.4 Pore water geochemistry and reaction-transport modelling

We analysed 16 pore water samples from GC 36_{fjord} for their dissolved constituents and the isotopic composition of DIC, and 15 samples (sediment + pore water) for the headspace methane concentration and methane carbon isotopes (Table 3). These data were plotted and compared to pore water data of core GC 51_{shelf} (Figure 5) from a seep setting in the Hola trough which was described in detail by Sauer et al. (2015).

Table 3: Results of pore water analyses of core GC 36$_{fjord}$.

Depth (cm)	PO_4^{3-} (µM)	SO_4^{2-} (mM)	NH_4^+ (µM)	HS^- (mM)	δ^{13}C- DIC (‰ V-PDB)	Depth (cm)	CH_4 (mM)	δ^{13}C- CH_4 (‰ V-PDB)
11	37.1	25.2	0.5	0.4	-11.9	25	0.0	
36	55.3	20.4	1.4	1.9	-9.8	50	0.1	
62	92.5	13.8	2.2	4.2	-18.4	75	0.1	
89	82.9	9.9	2.8	5.2	-18.7	100	0.1	
113	88.2	6.5	3.3	6.5	-19.2	125	0.2	-85.3
138	146.8	3.0	3.9	8.3	-17.9	150	0.3	-91.0
162	161.1	< 0.07	4.2	8.0	-18.4	175	1.0	
188	167.8	< 0.07	4.6	7.3	-15.5	200	2.7	-96.5
213	191.7	< 0.07	5.1	6.5	-8.9	225	4.0	-94.9
238	212.7	< 0.07	5.8	5.5	-8.6	250	6.5	-94.9
264	228.9	< 0.07	6.0	4.9	-6.3	275	5.7	-93.9
289	236.6	< 0.07	6.3	4.6	-5.5	300	6.9	-92.3
314	266.2	< 0.07	6.7	4.0	-2.6	325	7.6	-91.8
339	272.9	< 0.07	7.0	3.3	-2.8	350	5.9	-89.6
359	279.4	< 0.07	7.1	2.2	-1.9	365	5.3	-89.5
374	298.7	< 0.07	7.6	2.0	-1.2			

In core GC 36$_{fjord}$ sulphate concentrations decreased below detection limit at 162 cm depth. Methane concentrations were below 0.2 mM in the upper 125 cm of the sediment core and then increased downcore up to 7.6 mM in the deepest section cored (Table 3). Thus, the SMT spanned from 125 cm to 162 cm sediment depth. Coinciding with this depth interval was the peak in HS^- concentration of 8.3 mM. Upward and downward from the SMT, HS^- concentrations decreased gradually. The SMT depth in GC 51$_{shelf}$ was between 80 cm and 110 cm (Sauer et al., 2015), shallower than the depth in GC 36$_{fjord}$.

Pore water concentrations of ammonium and phosphate increased with depth in core GC 36$_{fjord}$ to values up to 7.6 mM and 299 µM, respectively, at the base of the core. Ammonium concentrations at the base of the core are more than 24 times higher in GC 36$_{fjord}$ compared to GC 51$_{shelf}$ (Sauer et al., 2015). Phosphate concentrations were also significantly higher in core GC 36$_{fjord}$ than in GC 51$_{shelf}$.

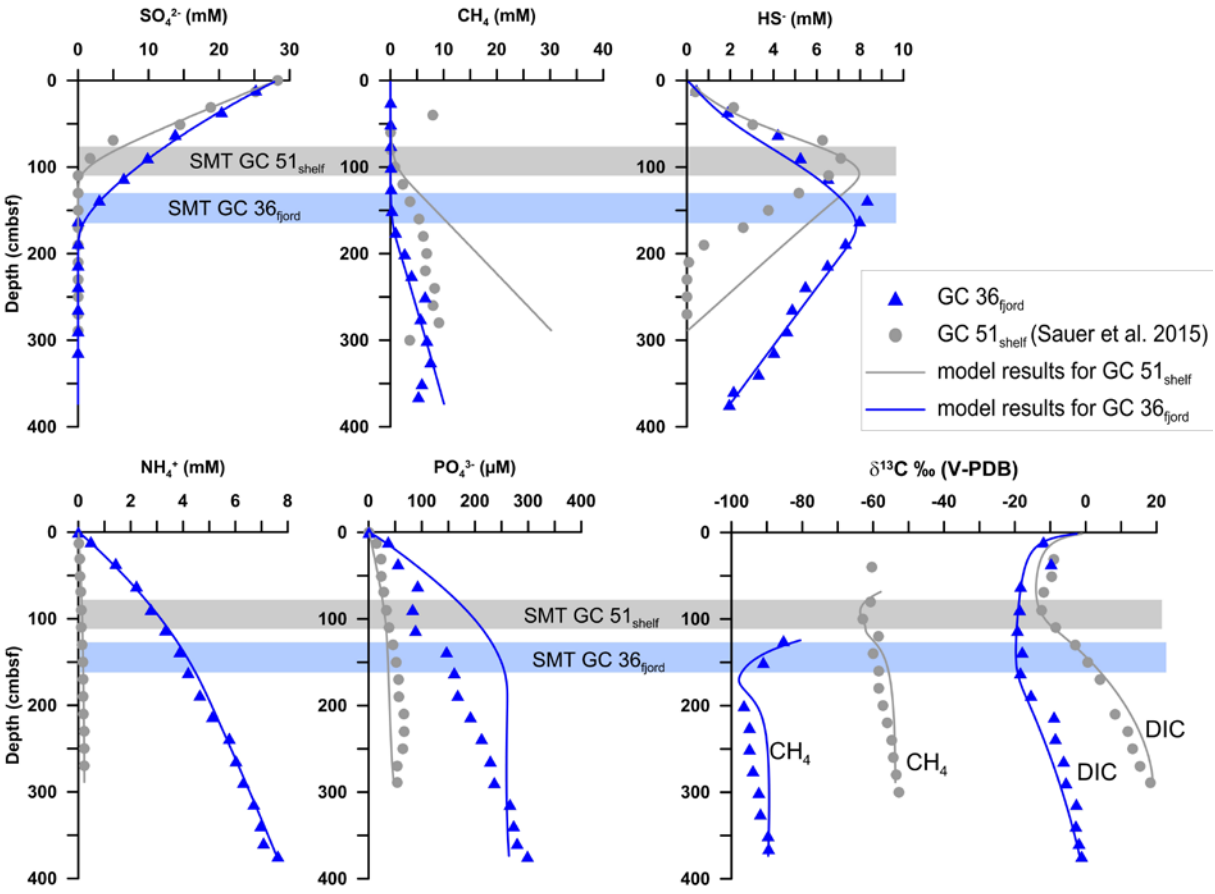

Figure 5: Pore water concentration profiles in core GC 36$_{fjord}$ from Ullsfjorden (blue triangle) and GC 51$_{shelf}$ from the Hola trough (grey dots, Sauer et al., 2015). The lines represent the fitted model results for both cores and the grey and blue shaded bands represent the depth of the sulphate-methane-transition (SMT) in core GC 51$_{shelf}$ and GC 36$_{fjord}$, respectively.

The δ^{13}C-CH$_4$ of GC 36$_{fjord}$ ranged from -96.5‰ to -85.3‰ (Table 3). The lowest value was at 200 cm depth and values increased upward through the SMT to -85.3‰ and downward as well to -89.5‰. In comparison, δ^{13}C-CH$_4$ values in GC 51$_{shelf}$ were around 30‰ higher than in GC 36$_{fjord}$ and ranged between -60‰ and -53‰ (Figure 5).

In GC 36$_{fjord}$ the lowest values of δ^{13}C-DIC (between -19.2‰ and -17.9‰) were found in the interval from 62 cm to 162 cm. Downward, below the SMT values increased up to -1.2‰ and upward to roughly -10‰ (Table 3). In GC 51$_{shelf}$ the lowest δ^{13}C-DIC value was -12‰. The same increasing trend as in GC 36$_{fjord}$ is observed below the SMT in GC 51$_{shelf}$, but δ^{13}C-DIC increased stronger with depth up to a value of +18‰ in GC 51$_{shelf}$ (Figure 5).

In general, our pore water model can satisfactorily fit the observed profiles except for the methane concentration profiles for both sites, the sulphide concentration profile at GC 51$_{shelf}$, and the

phosphate concentration profile at GC 36_{fjord} (Figure 5). Measurements of methane concentration were potentially affected by degassing during core recovery (Dickens et al., 2003). These measurements are therefore only minimum constraints of *in-situ* methane concentrations. The misfit between measured and modelled sulphide profiles at GC 51_{shelf} was potentially due to an additional sink for sulphide, precipitation of iron sulphide minerals, which was not considered in our model. The higher phosphate concentration at GC 36_{fjord} estimated by our model compared to the observation may reflect the variable C/P ratios in the organic matter throughout the burial history, which was assumed constant in our model.

4.5 Gas isotopes

We analysed two samples of core GC 36_{fjord} (200 cm and 365 cm sediment depth) for δ^2H of methane and the δ^{13}C of ethane, propane and butane. In both samples the δ^2H-CH_4 was very similar, -218‰ and -220‰ (Table 4). The δ^{13}C of the higher molecular weight hydrocarbons increased with increasing carbon number: methane (-96.5% to -89.5‰), ethane (-57.1‰), propane (-38.6‰ to -37.3‰), *n*-butane (-36.4‰ to -33.7‰). In GC 51_{shelf} δ^2H-CH_4 values (Sauer et al., 2015) were similar to those in GC 36_{fjord}. However, the δ^{13}C values of ethane, propane and *n*-butane were higher in GC 51_{shelf} by between 11‰ and 23‰.

Table 4: Results of isotopic analyses of methane, ethane, propane and butane of GC-36_{fjord}. All values of GC 51_{shelf} are from the study of Sauer et al. (2015).

	δ^2H (‰ V-SMOW)	δ^{13}C (‰ V-PDB)			
Sample	CH_4	CH_4 (C_1)	C_2H_6 (C_2)	C_3H_8 (C_3)	*n*C_4H_{10} (*n*-C_4)
GC 36-200 cm	-218	-96,5	-	-37,3	-36,4
GC 36-365 cm	-220	-89,5	-57,1	-38,6	-33,7
GC 51-140 cm	-218	-60,0	-34,4	-14,9	-22,4
GC 51-220 cm	-225	-56,1	-36,5	-16	-22,5
GC 51-300 cm	-223	-52,7	-34,4	-12,1	-24,8
GC 52-140 cm	-191	-54,4	-33,7	-9,5	-25,2
GC 52-180 cm	-212	-53,5	-34,6	-13,2	-26,3
GC 52-240 cm	-222	-52,3	-34,0	-7,0	-29,1

5 Discussion

5.1 Organic matter source

We consider three possible sources of the sedimentary organic matter in the studied gravity cores: marine organic matter (MOM), fresh terrestrial organic matter (TOM) and fossil organic matter from weathered or glacially eroded bedrock (Tyson, 1995). For a first order discrimination between MOM and TOM we use the $\delta^{13}C$-C_{org} and the C/N ratio (e.g. Meyers, 1994; Hall and McCave, 1998; Schubert and Calvert, 2001; St-Onge and Hillaire-Marcel, 2001; Knies et al., 2003; Knies and Martinez, 2009; Yu et al., 2010). Marine algae typically have atomic C/N ratios between 4 and 10, mostly exhibiting the "Redfield" carbon to nitrogen ratio of 7 (Meyers, 1994).

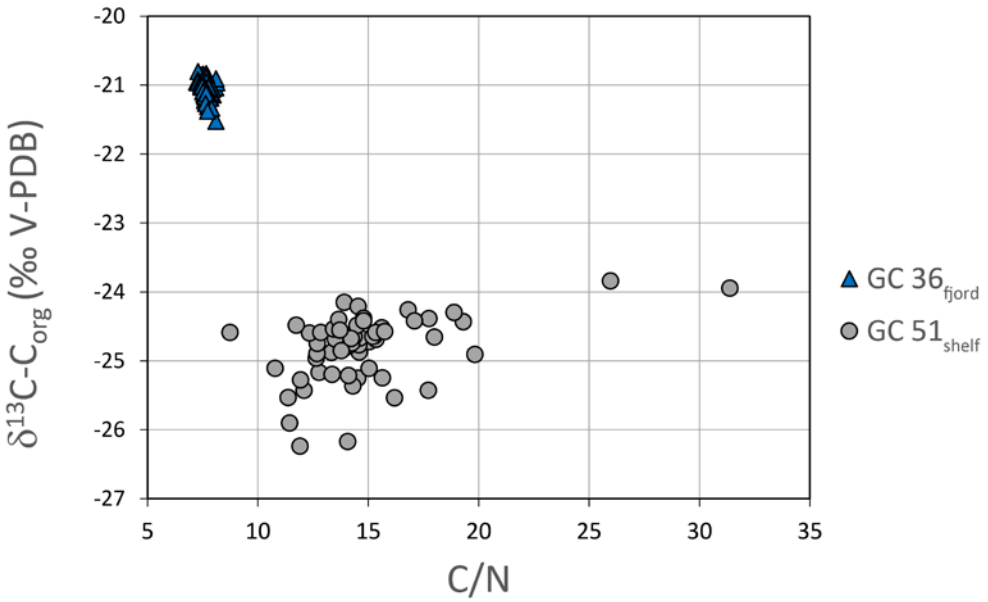

Figure 6: Plot of sedimentary $\delta^{13}C$-C_{org} against C/N ratio of cores GC 36_{fjord} (blue triangles) and GC 51_{shelf} (grey dots).

Generally, in freshly deposited sediments this value is slightly higher (9-10) due to the preferential loss of nitrogen during organic matter degradation in the water column (Fenchel et al., 2012b). In contrast, the C/N ratio of vascular land plants is ≥ 20 (Meyers, 1994).

The $\delta^{13}C$ value of TOM is generally lighter than that of MOM. For the $\delta^{13}C$ of TOM one has to differentiate between C3 and C4 plants, because they discriminate differently against $^{13}CO_2$ (Farquhar et al., 1989). However, at high latitudes the influence of C4 plants is minor (e.g. Teeri and

Stowe, 1976). TOM derived from C3 plants has $\delta^{13}C$ values that commonly range between -23 and -35‰ with an average of -27‰ (Meyers, 1994), whereas MOM normally shows heavier isotopic values between -13‰ and -31‰ (Tyson, 1995). Rau et al. (1982) found an average $\delta^{13}C$ value of -20.9‰ for marine phytoplankton at latitudes higher than 62°N and Knies et al. (2003) reported a very similar value of -20.3‰ for northern Norwegian coastal MOM.

The sedimentary organic matter in Ullsfjorden is dominated by marine phytoplankton (Figure 6) as the average $\delta^{13}C$-C_{org} in core GC 36_{fjord} of -21‰ coincides very well with the values found for high northern latitude marine phytoplankton (Rau et al., 1982; Schubert and Calvert, 2001). Also, the average C/N ratio (7.7) falls well within the MOM range (Figure 6). The vegetation cover of the hinterland seems to play a minor role in supplying organic matter to the fjord. This is further supported by the constantly low magnetic susceptibility, which commonly suggests a dominance in marine biogenic material in the sediment (e.g. Hounslow and Maher, 1999) (Figure 3). Since there is no significant variation in the $\delta^{13}C$-C_{org} and C/N ratio within GC 36_{fjord} (Figure 4 and 6), the organic matter source supplied to the sediment has probably stayed constant over the last approximately 4000 years.

In contrast, the sedimentary organic matter of core GC 51_{shelf} shows a much stronger terrestrial influence with a higher average C/N value of 14.8 and lower $\delta^{13}C$ values of on average -24.8‰ (Figure 6). Moreover, there is considerably more variation in both C/N and $\delta^{13}C$ in GC 51_{shelf} than GC 36_{fjord} suggesting changes in the organic matter source over time. Yet we found no correlation between the two variables C/N and $\delta^{13}C$-C_{org} in core GC 51_{shelf} ($r^2 < 0.2$) which points to a mixing of more than two end members with different $\delta^{13}C$ and C/N signatures. The poor correlation and the lack of well constrained end members make a quantification of the different C_{org} sources in GC 51_{shelf} difficult.

Besides the common organic matter sources considered, there are two intervals from GC 51_{shelf} that demonstrate abnormal geochemical signatures which may reflect organic matter from less common sources (Figure 4, grey bands). These two intervals with the most prominent changes in $\delta^{13}C$ and/or

C/N in core GC 51$_{shelf}$ are 35-45 cm (drop in δ^{13}C-C$_{org}$ to -26‰) and 282-292 cm (increase in C/N ratio to 31 and in δ^{13}C-C$_{org}$ to -24‰). The latter depth interval also corresponds to a peak in C$_{org}$ of up to 1.9% (Figure 4). The first interval could be explained by either an increased proportion of TOM (assumed average -27‰), or a contribution of methanogenic/methanotrophic microbial biomass which can be very depleted in δ^{13}C with values up to -120‰ of some archaeal lipids (Yoshinaga et al., 2015). Yoshinaga et al. (2015) reported, for example, a substantial contributions of AOM related biomass to C$_{org}$ in sediment cores from cold seep sites off Pakistan. The Hola trough also hosts cold seeps with high methane fluxes that can promote microbial methanotrophic activity (Sauer et al., 2015).Thus, a contribution of microbial biomass may be responsible for the lighter δ^{13}C values in the upper interval of core GC 51$_{shelf}$ (Figure 4). Furthermore, there is no increase in C/N ratio in this interval which would be expected if an increased TOM proportion was responsible for lighter δ^{13}C values. Bacterial biomass has a C/N ratio of around 5 (Fenchel et al., 2012a), so it cannot be distinguished from MOM based on the C/N ratio.

For the second interval (282-292 cm), the organic matter sources are less clear. Elevated C/N values of up to 31 would normally indicate high input of TOM at that time. However, the δ^{13}C-C$_{org}$ values do not fit this interpretation. The heavier isotopic values of up to -23.8‰ indicate weaker terrestrial organic matter input. A possible explanation might be an interval dominated by fossil organic matter derived from the erosion of organic rich bedrock in the vicinity. The C/N ratio usually increases with progressive decomposition of the organic matter due to the preferential removal of nitrogen by the degradation of high-N compounds during diagenesis (Fenchel et al., 1998; Lehmann et al., 2002). Thus, old organic matter should have higher C/N ratios. Early Cretaceous rocks with high organic carbon contents were drilled about 30 km away from the present study area on the shelf and were found at only 10 m depth below the seafloor (Hansen et al., 1992; Smelror et al., 2001). Thus, if they outcrop in the vicinity they could have provided old organic matter to the shelf, most likely by glacial erosion. The other possibility of preserving high C/N ratios in the organic matter, with δ^{13}C ratios closer to the marine range, is a period of high productivity as described by Meyers (1994) from the

region offshore Namibia. Here elevated C/N ratios are attributed to high rates of productivity because land derived organic matter could be excluded. Although we cannot confirm the organic matter source within the second interval, there is an obvious change in organic matter supply, either from ancient organic matter or a period of high productivity. As most of the core GC 51_{shelf} represents sedimentation in a dynamic glacial to post glacial environment with contribution of sediment from glacial erosion of the hinterland we favour the interpretation of ancient eroded C_{org} in this interval of GC 51_{shelf}.

5.2 Organic matter burial and sediment characteristics

Core GC 36_{fjord} comprises a massive mud deposited in an open marine environment during the last ca 4000 years. Grain size and magnetic susceptibility remain rather constant except for a thin interval at 140 cm (Figure 4, blue band). This interval shows a higher fraction of coarse grained material, higher density, less C_{org} and N_{tot}. This can be explained by a higher proportion of clastic material with higher density and coarse grain size in this interval which dilutes the marine components. We assume that this interval is composed of reworked sediments. Other than the local minima in C_{org} at 140 cm GC 36_{fjord} shows a regular C_{org} profile with decreasing concentration with depth likely due to early diagenetic degradation (Hedges and Keil, 1995). The constant C/N ratio shows that there is no preferential nitrogen removal during early diagenesis in these sediments, as opposed to observations in the water column (Fenchel et al., 2012b). Despite a decreasing C_{org} content with depth, the overall C_{org} (average >2%) is high.

In comparison, the C_{org} content from GC 51_{shelf} is generally low but increasing gradually with depth. The C_{org} profile of GC 51_{shelf} correlates with grain size distribution (Figure 7): the C_{org} content increases with depth along with the increase in the fine fraction, except for the interval 282-292 cm with a C_{org} peak. Thus, we assume the organic matter in the sediment is associated with the fine grained fraction (de Haas et al., 2002). This is supported by findings of Bianchi and Bauer (2011) that 90% of river and estuarine derived organic carbon entering the coastal zone is associated with mineral matrices in organo-clay aggregates.

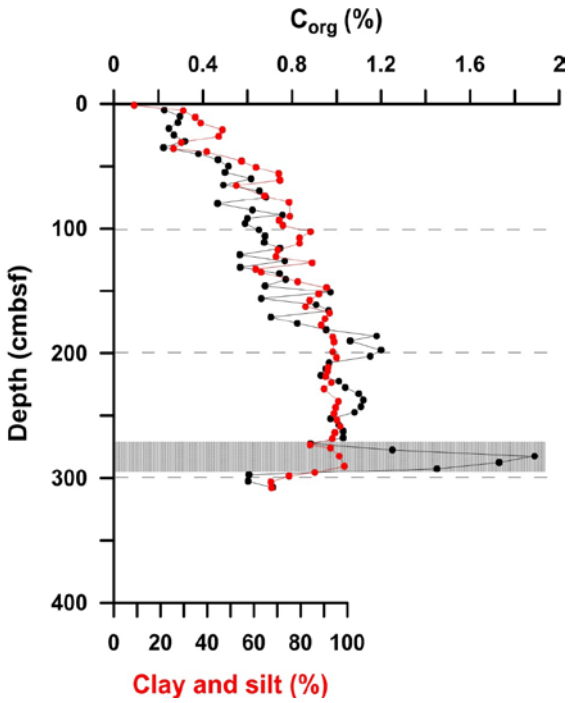

Figure 7: Comparison of C_{org} content and the sum of the clay and silt fraction of GC 51_{shelf}.

The decrease in the fine fraction towards the top of the core might be a result of increased erosion by strong bottom currents in the Hola trough since the deglaciation (Bøe et al., 2015). An increase in current velocity has also been hypothesized for Malangsdjupet (a cross-shelf trough north of the Hola trough) during the Holocene due to changes in marine currents along the coast (Elvsborg, 1979). The establishment of modern oceanographic conditions in the Nordic Sea with the Norwegian Atlantic Current (NAC) and the Norwegian Coastal Current (NCC) eroding and winnowing fine material and leaving a lag deposit of sand, gravel and boulders on the shelf probably started around the Bølling Allerød interstadial (Bøe et al., 2015 and references therein). The general sedimentary succession of northern Norwegian shelf is the deposition of basal tills during the last glaciation that discordantly overlie Cretaceous sedimentary rocks. Fine-grained glaciomarine sediments and Holocene sand cover the till (Bøe et al., 2009). The lowermost 12 cm of GC 51_{shelf} is poorly sorted (Figure 3) with some angular clasts up to 2 cm in diameter (Figure 8) suggesting a glacial origin, either a basal till or glaciomarine sediment (Elvsborg, 1979; Forwick and Vorren, 2009).

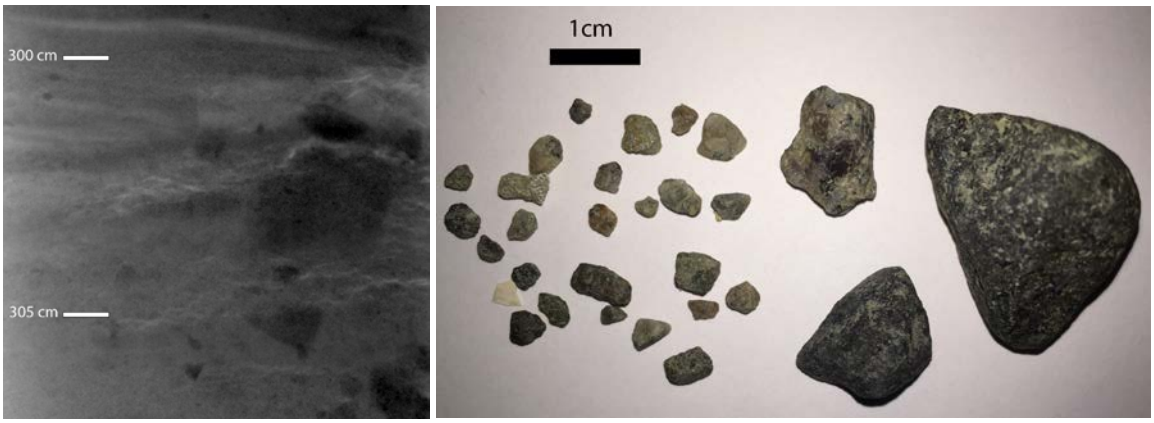

Figure 8: X-ray image of the lower part of GC 51$_{shelf}$ (left) and photo of the grains > 2mm contained in this section (right).

The ^{14}C age determined on the foraminifera at 300 cm (around 40 cal ka BP), which lies within the glacial sediment is not regarded as the actual depositional age, because the material is probably re-deposited older marine sediment. Therefore, we estimate the bottom of the core to be the age of the till which deposited when the ice retreated from this area. This is estimated to be around 18-17.5 cal ka BP by Vorren et al. (2015), who ascribed a grounding zone wedge just next to the core site GC 51$_{shelf}$ to the Flesen event dated to ca. 14.5 ^{14}C ka/17.5 cal ka BP (Vorren and Plassen, 2002). Laminated finer grained material covering the till from 200 to 80 cm in core GC 51$_{shelf}$ was probably deposited from sediment-laden meltwater plumes during deglaciation (Vorren et al., 1984). Compared to present current strength, the strength of the along-slope current was generally lower during the glacial (e.g. Laberg et al., 2005) allowing the deposition of finer grained material. Furthermore, the sedimentation rate was much higher because of the proximity of the glacier front which represented an important sediment source. But since post-glacial times winnowing along the shelf and upper slope by the Norwegian Atlantic Current is the dominant erosional process (Vorren et al., 1984; Laberg et al., 2005; Bellec et al., 2012). Present estimates of bottom current speed are up to 0.7 m s^{-1} (Bøe et al., 2009) and at this speed pebbles up to 3 mm in diameter can be eroded and boulders transported as bedload (Johnson et al., 1982). This formed a lag deposit which resulted in the pebbly sand we observed as the very top layer in the Hola trough.

Foraminifera from 3-4 cm sediment depth were dated to around 3.5 cal ka BP, which supports the notion that the surface sediments were eroded. This also implies that C_{org} burial in this area is

presently absent. Any MOM from primary production must be remineralised in the water column or transported off the shelf towards the shelf break and further downslope along with the fine-grained sediment fraction (de Haas et al., 2002; Bøe et al., 2015).

Table 5: Average values of sedimentation rate (SR), dry bulk density (DBD) and C_{org} content used to calculate C_{org} accumulation rate (AR). The intervals are determined by the depths of ^{14}C dating.

Core	Interval (cm)	approximate Time interval (cal years BP)	SR (cm ka $^{-1}$)	DBD (g cm^{-3})	average C_{org} (%)	Bulk AR (g cm^{-2} ka^{-1})	C_{org} AR (gC cm^{-2} ka^{-1})
GC 36 fjord	0 - 82.5	present - 875	88	0.28	2.54	24.50	0.621
	82.5 - 128	875 - 1,231	129	0.54	2.29	69.32	1.585
	128 - 225	1,231 - 2,005	124	0.69	2.13	85.40	1.821
	225 - 364	2,005 - 3,905	73	0.70	2.07	51.45	1.066
	0 - 364	**present - 3,905**	**92**	**0.6**	**2.2**	**55.20**	**1.214**
GC 51 shelf	3.5-108.5	3,481 - 15,613	8.7	1.38	0.48	12.01	0.058
	108.5-312	15,613 - 18,000	80	1.10	0.96	88.00	0.845

From the C_{org} profile and the general coarsening upward (Figure 7) we suggest that there has been a progressive decrease in the deposition of fine grained sediments and associated organic matter during the last 15 ka. The shelf area apparently played a more important role in C_{org} burial during the last glacial than during the present interglacial. Similar findings of glacial-interglacial variations of C_{org} burial have been observed in other areas along the NW European continental slope (Hall and McCave, 1998). The C_{org} deposition on the slope has decreased in the past 20 ka to less than half, from late glacial to Holocene values: from 0.06 g C cm^{-2} ka $^{-1}$ to less than 0.03 g C cm^{-2} ka $^{-1}$ (Hall and McCave, 1998).

Our C_{org} accumulation rates estimated for Ullsfjorden (0.6-1.8 g C cm^{-2} ka $^{-1}$, Table 5) are similar to those from other high northern latitude fjords. In Storfjorden (Spitsbergen) and the Saguenay fjord (Quebec) C_{org} accumulation rates are between 1.2 to 4 g C cm^{-2} ka $^{-1}$ (Winkelmann and Knies, 2005) and around 3 g C cm^{-2} ka $^{-1}$ (St-Onge and Hillaire-Marcel, 2001). A recent paper by Smith et al. (2015) further highlights the role of fjords as a global C_{org} sink. They report a global average C_{org} accumulation rate for fjords of 5.4 g C cm^{-2} ka^{-1} and that 11% of annual marine carbon is buried in fjord sediments. The C_{org} accumulation rate that we estimated for Ullsfjorden lies at the lower end of C_{org} accumulation rates that Smith et al. (2015) determined for fjords worldwide, but it is still multiple

times higher than accumulation rates determined for site GC 51_{shelf} located on the shelf in the Hola trough.

5.3 Organic matter degradation: sulphate reduction and methanogenesis

In order to quantify the degradation of organic matter in shelf and fjord sediments by particulate organic carbon sulphate reduction (POCSR) and methanogenesis (ME), we applied a transport-reaction model to the key pore water profiles (Figure 5). By fitting sulphate, ammonium and phosphate profiles, we are able to estimate the overall organic matter degradation rate through the two reactions. Our model reveals an order of magnitude higher POCSR rate for GC 36_{fjord} than for GC 51_{shelf} and only slightly higher ME rates at the GC 36_{fjord} site (Figure 9 and Table 6). The higher organic matter degradation rate at GC 36_{fjord} is potentially fuelled by the higher input of labile MOM at this site as suggested by its sediment geochemistry (C_{org} content, C/N ratio and $\delta^{13}C$-C_{org})(Figure 4) and the high accumulation rate of C_{org} (Table 5).

Even though the organic matter burial and decomposition rates are significantly higher in GC 36_{fjord}, we observed a shallower SMT in GC 51_{shelf}. Our model results suggest that 96.9% of the depth-integrated sulphate reduction at GC 51_{shelf} is mediated by AOM (Table 6) indicating a strong methane supply at this site. Methane which is utilized during AOM can be produced by organic matter degradation through in-situ methanogenesis or from sources deeper than the depth we considered in the model (the core length). Our model estimated that only 3.6% of the methane carbon is produced by in-situ ME at GC 51_{shelf} (Table 6). Thus, most of the methane that contributes to AOM at this site comes from a different source. The heavier carbon isotopic signature of methane at the bottom of GC 51_{shelf} (Figure 5) suggests methane input from thermogenic sources (Sauer et al., 2015).

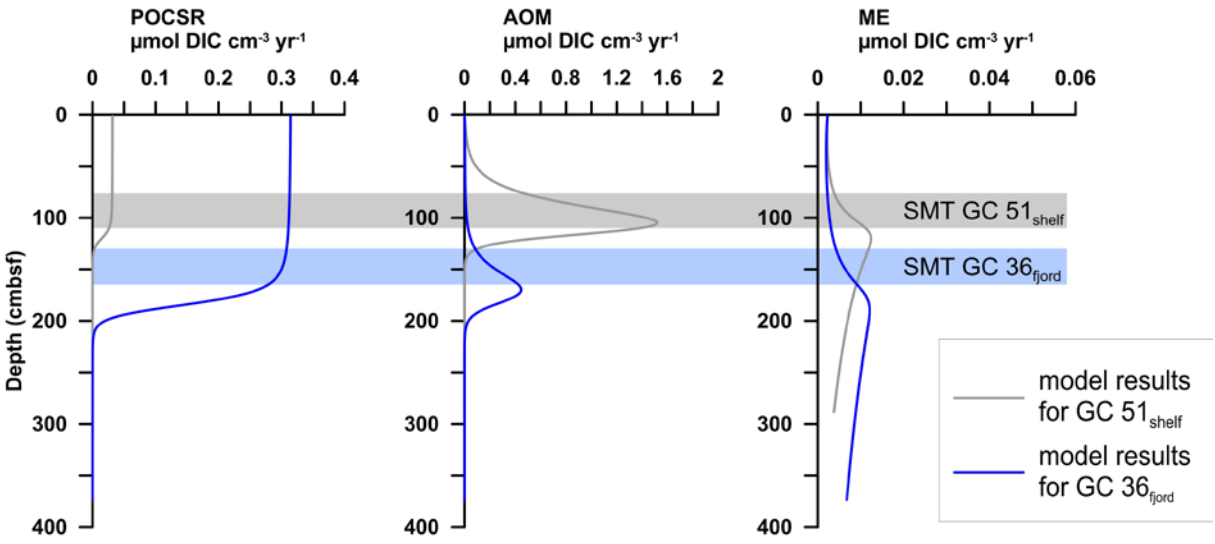

Figure 9: Modelled rates of anaerobic oxidation of methane (AOM), methanogenesis (ME) and particulate organic carbon sulphate reduction (POCSR) at sites GC 36$_{fjord}$ and GC 51$_{shelf}$. The grey and blue shaded bands represent the depth of the sulphate-methane-transition (SMT) in cores GC 51$_{shelf}$ and GC 36$_{fjord}$, respectively.

Our model estimates a ca. 3 times higher AOM rate at GC 51$_{shelf}$ compared to the rate at GC 36$_{fjord}$ (Table 6). The AOM rate in Hola is higher but of the same magnitude as the rates estimated from a deep water site (ca. 1200 m) west of Svalbard which is also an active methane seep site (Hong et al., 2016 accepted). The rapid methane consumption rates suggest that AOM can effectively prevent methane from leaking to the overlying bottom seawater in the fjord and at site GC 51$_{shelf}$ on the shelf. However, recent studies in the Hola trough also reveal active seeps where gas is released to the water column due to methane-rich fluid ascent along certain pathways (Chand et al., 2008; Sauer et al., 2015).

Table 6: Depth-integrated rates of AOM, POCSR and ME in units of µmol DIC cm^{-2} yr^{-1}.

	SMT depth (m)	**AOM**	**POCSR**	**ME**	**Total SR[1] (fraction of sulphate reduction coupled to AOM)**
GC 36$_{fjord}$	1.62	19.2	56.8	2.5	47.6 (40.4%)
GC 51$_{shelf}$	1.10	57.4	3.7	1.8	59.2 (96.9%)

[1] µmol sulphate *cm^{-2} yr^{-1}*

Based on our model results, we propose that the different organic matter degradation pathways, POCSR or ME, and the overall decomposition rate of organic matter can explain the different δ^{13}C-DIC

patterns between the two sites. At GC 36_{fjord}, the overall organic matter decomposition rate is 59.3 µmol cm^{-2} yr^{-1} (sum of POCSR and ME rates in Table 6) while at GC 51_{shelf} the rate of 5.5 µmol cm^{-2} yr^{-1} is an order of magnitude lower. POSCR is responsible for 96% of the overall organic matter degradation at GC 36_{fjord} while only 67% of organic matter is degraded through POCSR at GC 51_{shelf}. POCSR only causes negligible isotopic fractionation on carbon; in other words, the DIC produced by POCSR has the same carbon isotopic signature as the organic matter (Presley and Kaplan, 1968). Methanogenesis, on the other hand, has a larger isotopic fractionation effect on carbon (Whiticar, 1999); thus resulting in a stronger ^{13}C enrichment in DIC than organic matter degradation. At GC 36_{fjord}, POCSR dominates DIC production and therefore results in the carbon isotopic signature similar to the signature of the marine organic matter (-21‰) at and above the SMT. At GC 51_{shelf}, ME contributes 33% of DIC to the entire pool, whose size also is supposed to be much smaller than the DIC pool at GC 36_{fjord}. The influence of DIC from ME on the $\delta^{13}C$-DIC becomes more obvious below the SMT at GC 51_{shelf} which could explain the stronger shift to positive $\delta^{13}C$-DIC values at site GC 51_{shelf} compared to GC 36_{fjord} (Figure 5).

An alternative explanation for isotopically heavier DIC in GC 51_{shelf} than in GC 36_{fjord} is the contribution of DIC from the deep-sourced fluid in the Hola trough. Sauer et al. (2015) reported signs of biodegradation of propane and n-butane in GC 51_{shelf} based on their $\delta^{13}C$ values. Several studies have shown a relationship between anaerobic hydrocarbon degradation and heavy $\delta^{13}C$ DIC or CO_2 values (Pallaser, 2000; Jones et al., 2008; Etiope et al., 2009; Milkov, 2011). This relationship is explained, firstly, by the formation of CO_2 due to the degradation of the higher-molecular-weight hydrocarbons and, secondly, by the subsequent secondary methanogenesis using the previously produced CO_2 which enriches the remaining CO_2 pool in ^{13}C (Jones et al., 2008). This can lead to $\delta^{13}C$ values of CO_2 as positive as +27‰, as reported in a biodegraded petroleum accumulation in the West Siberian Basin (Milkov, 2010). The ^{13}C enrichment in CO_2 requires anaerobic conditions, because methanogenesis does not take place under aerobic conditions. Thus, the ^{13}C enriched DIC at depth in core GC 51_{shelf} could also be related to the contribution of isotopically heavy DIC from the deeper

fluids.

5.4 Gas sources in Ullsfjorden and the Hola trough

This section highlights the differences in gas sources between Ullsfjorden and the Hola trough (Figure 10 and 11). Hydrocarbons in the Hola trough are thermogenic with only a minor contribution of microbial methane (Sauer et al., 2015). This microbial methane can originate either from in-situ methanogenesis, as shown by our pore water modelling, or secondary methanogenesis resulting from higher hydrocarbon degradation. In Ullsfjorden, we suggest a purely microbial source of methane. Even the higher hydrocarbons are probably formed by microbial processes as indicated by their light $\delta^{13}C$ values.

Our gas isotope results show a distinct difference in gas source between the Hola trough and Ullsfjorden. The predominantly deeper thermogenic source of hydrocarbons in the Hola trough is evident in Figure 11 but a microbial contribution is suggested from Figure 10 (for details see Sauer et al., 2015). An additional source of microbial methane derives from the alternative interpretation of the isotopically heavy DIC in core GC 51_{shelf} being caused by anaerobic hydrocarbon degradation. The formation of isotopically heavy DIC in the deep reservoir requires secondary methanogenesis (Jones et al., 2008). Thus, the proportion of microbial methane in GC 51_{shelf} could be attributed to either primary methane production from in-situ methanogenesis and/or to secondary methane production through degradation of higher hydrocarbons by microbes. The relationship of anaerobic hydrocarbon degradation and secondary methanogenesis that results in ^{13}C enriched fluids has been discussed in several studies which found evidence of this process recorded in high $\delta^{13}C$ values of carbonates or CO_2 gas (Dimitrakopoulos and Muehlenbachs, 1987; Pallaser, 2000; Crémière et al., 2012; Crémière et al., 2013).

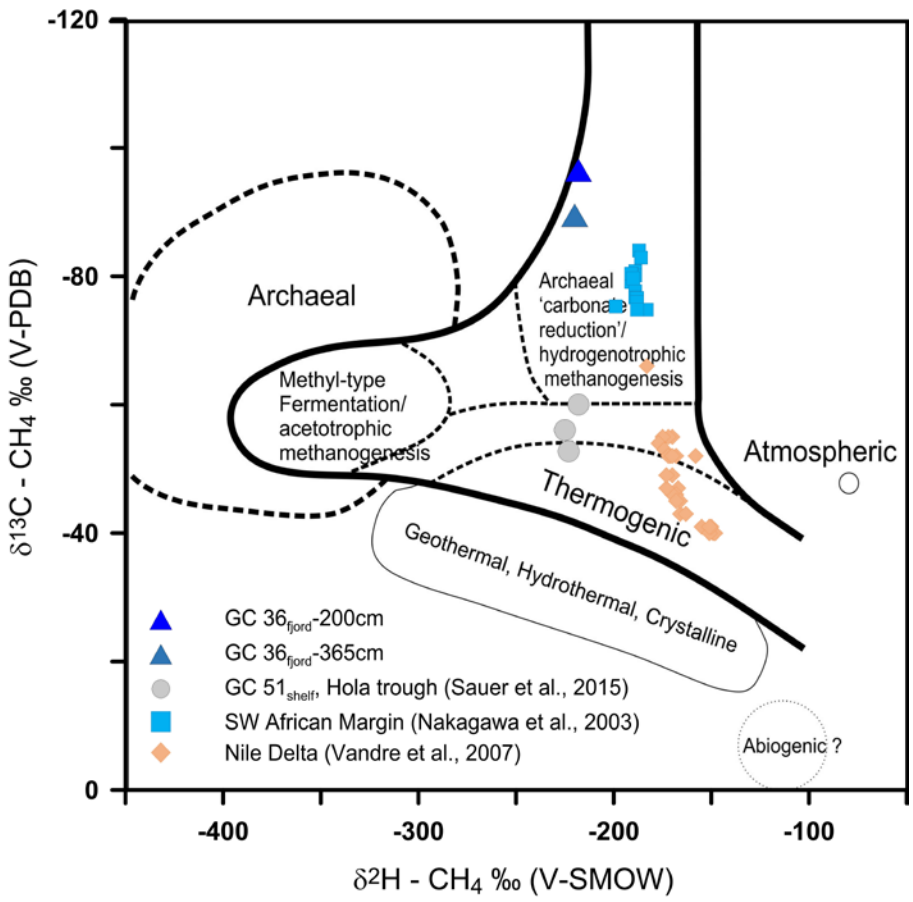

Figure 10: Plot of $\delta^{13}C$ of methane against $\delta^{2}H$ of methane. The fields of different methane sources are based on Whiticar (1999). Analyses of samples from GC 36_{fjord} (blue triangles) plot clearly in the field of hydrogenotrophic methanogenesis.

In Ullsfjorden the contribution of thermogenic gases was considered unlikely (Plassen and Vorren, 2003b) which is strongly supported by our results. The methane carbon isotopic values of the Ullsfjorden samples are all below -80‰ and thus well within the range of microbial methane (Whiticar, 1999) (Figure 10). The two main pathways of microbial (archaeal) methanogenesis are via carbonate reduction, also called hydrogenotrophic methanogenesis, or acetotrophic methanogenesis. The very light $\delta^{13}C\text{-}CH_4$ values of the Ullsfjorden gas samples down to -96.5‰ clearly favour hydrogenotrophic over acetotrophic methanogenesis in the fjord sediments (Figure 10). Depth profiles of $\delta^{13}C$ of methane and DIC in the methanogenic zone below the SMT in GC 36_{fjord} are in accordance with hydrogenotrophic methanogenesis. $\delta^{13}C\text{-}CH_4$ and $\delta^{13}C\text{-DIC}$ show the same gradients in this part of the core (200 cm-380 cm, Figure 5), because methane is produced from DIC with a constant fractionation factor (Whiticar, 1999). The parallel increase in both $\delta^{13}C\text{-}CH_4$ and $\delta^{13}C\text{-DIC}$ with depth in GC 36_{fjord} is caused by a progressive enrichment of ^{13}C in the remaining DIC pool,

also causing progressive ^{13}C enrichment in the produced methane.

We detected ethane, propane and butane in Ullsfjorden sediments, which so far has been considered as an indication of thermogenic gas (e.g. Bernard et al., 1977; Pohlman et al., 2005). The microbial origin of these higher hydrocarbons has, however, been proposed in earlier studies of incubations of sediment slurries (Oremland et al., 1988), in deep marine sediments from the south eastern Pacific (Hinrichs et al., 2006), in Texas continental shelf and slope sediments (Bernard et al., 1978), and in shallow marine sediments offshore Indonesia (Bernard et al., 2013). Based on our $\delta^{13}C$ values of ethane and propane (Figure 11) we suggest that also the higher molecular weight hydrocarbons in the Ullsfjorden sediments were formed by microbial processes. Figure 11 shows that the isotopic composition of gases from Hola and Ullsfjorden plot in distinctly different places. The Hola samples group together with data from other localities of thermogenic gas (Katz et al., 2002; Pohlman et al., 2005; Vandré et al., 2007) whereas the sample from Ullsfjorden groups together with samples of reported microbial origin (Nakagawa et al., 2003; Bernard et al., 2013).

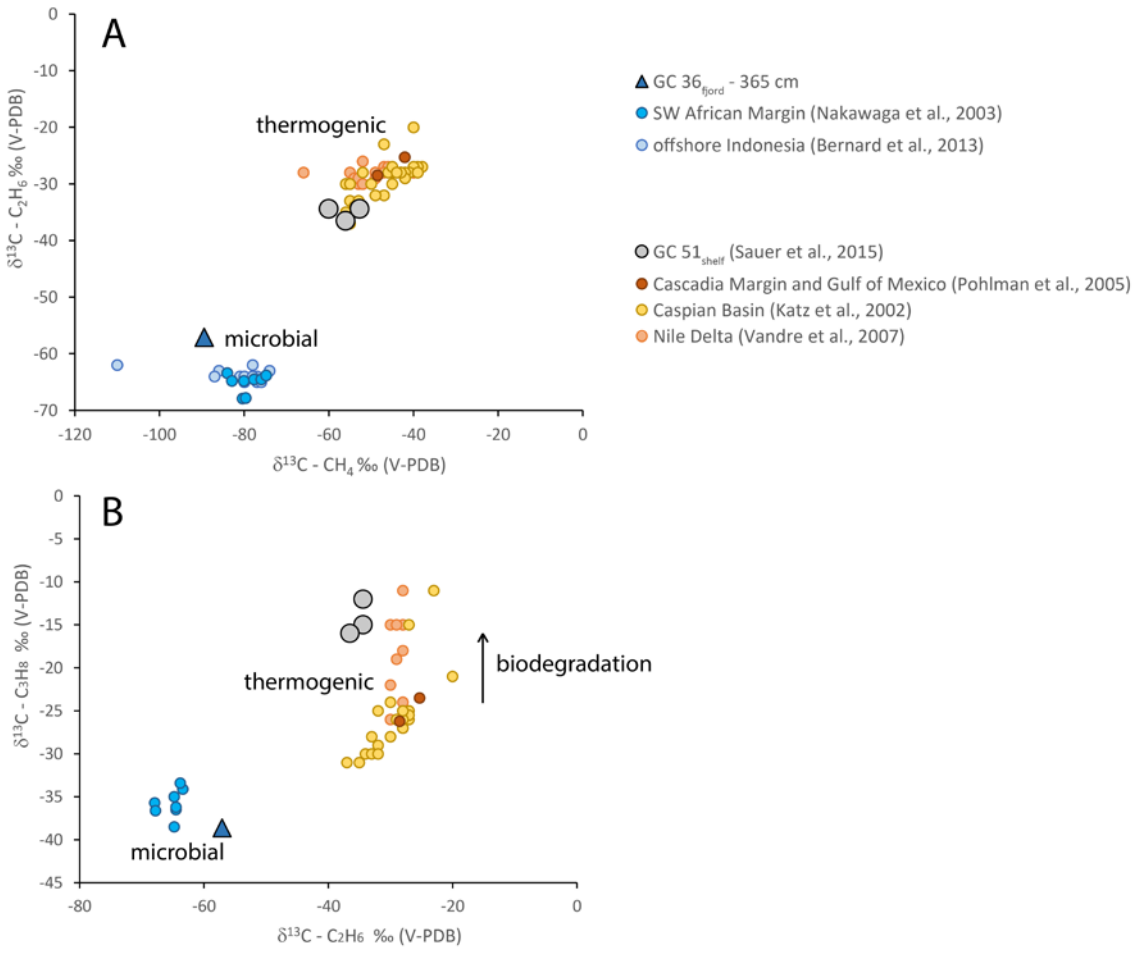

Figure 11: A) Plot of δ^{13}C-methane versus δ^{13}C-ethane and B) Plot of δ^{13}C-ethane versus δ^{13}C-propane. In both plots we compare the gas isotope data from Ullsfjorden to data from the literature (Katz et al., 2002; Nakagawa et al., 2003; Pohlman et al., 2005; Vandré et al., 2007; Bernard et al., 2013; Sauer et al., 2015)

The ethane δ^{13}C values of Ullsfjorden gas are much lighter than is known and accepted for natural thermogenic gas (Bernard et al., 2013). In the compilation of thermogenic gas by Milkov (2011) the δ^{13}C values of ethane range between -40‰ and -14‰, while ethane from Ullsfjorden has a δ^{13}C-C_2 of -57‰. Ethane with a light isotopic composition has also been reported by Bernard et al. (2013) and Nakagawa et al. (2003). Their samples from shallow sediments offshore Indonesia and the SW African margin, respectively, exhibit δ^{13}C-C_2 values between -68‰ and -54‰ and they propose a purely microbial origin to the gas. Moreover, the δ^{13}C values of propane from the Ullsfjorden gas samples are -37.3‰ and -38.6‰. These values are also lighter than the range of thermogenic gas samples plotted in Figure 11B. There are no isotopic values of potential microbial butane in the literature yet. However, we assume that also the butane in the Ullsfjorden sediments is of microbial origin, because

we are not aware of any mechanism that could result in a gas mixture of microbial methane, ethane and propane, and thermogenic butane.

6 Implications and conclusion

Burial of organic carbon in marine sediments is an important part of the carbon cycle; especially in shelf and fjord settings, where significant amounts of organic carbon are sequestrated. In this study, we investigated two gravity cores from northern Norway, GC 51_{shelf} from the Hola trough on the continental shelf offshore the Vesterålen Islands and GC 36_{fjord} from Ullsfjorden, to understand the dynamics of supply and burial of organic matter in these settings (Table 7).

In the Hola trough, geochemical properties of organic matter ($\delta^{13}C$-C_{org} and C/N ratios) suggest the dominance of terrestrial organic matter delivery to the shelf. C_{org} accumulation in the Hola trough has been decreasing continuously since the last glacial as a result of both low organic matter supplies and erosional ocean bottom currents which prevent the deposition of the fine-grained-sediment-associated organic matter. Therefore, the continental shelf offshore the Vesterålen Islands, and potentially the majority of the Norwegian shelf north of the Lofoten Islands, play only a minor role in C_{org} sequestration as all these areas are presently characterized by an erosional sedimentary regime (Bellec et al., 2012). However, during deglacial times the situation was different. Based on our study of GC 51_{shelf}, the sedimentation rates, fine grained fraction and organic matter content where higher during deglacial times causing higher rates of C_{org} accumulation than at present.

In Ullsfjorden, the high organic matter content and fast burial were sustained by the constant supply of marine organic matter from primary production over the last 4 ka. In light of previous studies of C_{org} sedimentation and burial, GC 36_{fjord} confirms the high rates of C_{org} burial in fjords supporting the view that fjords are hot spots of C_{org} accumulation (Keil, 2015; Smith et al., 2015). This is supported by a compilation of CO_2 air-sea gas exchange measurements by Chen et al. (2013), stating that the majority of fjords are a sink of atmospheric CO_2.

The difference in sedimentation dynamics and C_{org} accumulation between the fjord and shelf setting

strongly influences the early diagenetic processes in the sediment. As our model assessment on pore water profiles suggests, an order of magnitude more organic matter is degraded through sulphate reduction in the fjord than in the Hola trough. This is not surprising given the abundant labile marine organic matter supplied to the fjord sediment. Nonetheless, the SMT in the Hola trough is shallower than at the fjord site suggesting a faster sulphate turnover through AOM. Our model estimates that only a small fraction of AOM in the Hola trough is sustained by methane produced from in-situ methanogenesis. Instead, the majority of AOM at this location is fuelled by methane from a deeper thermogenic source (Sauer et al., 2015). The methane in Ullsfjorden is proposed to originate exclusively from microbial processes sustained by the high input of C_{org} from settling MOM. Even the ethane and propane detected in our samples can be of microbial origin as suggested by their stable carbon isotopic signatures.

The investigation of gas sources and early diagenetic processes highlights the different carbon sources in the two settings. In Ullsfjorden the carbon used by microbes for biogeochemical reaction is provided by settling organic matter from above, whereas on the Vesterålen shelf most of the carbon is provided by ascending methane from below.

Table 7: Summary of the main sedimentological and organic geochemical characteristics of core GC 36$_{fjord}$ and GC 51$_{shelf}$.

		GC 36$_{FJORD}$	**GC 51$_{SHELF}$**
SEDIMENTARY REGIME AND C_{ORG} BURIAL	Average SR	**High (73-129 cm ka^{-1})**	Low (9-80 cm ka^{-1})
	Grain size	Silt	Silt to sand
	C_{org} (%)	**High (1.5-3%)**	Low (0.2-1.9%)
	OM source	Dominantly marine	Dominantly terrestrial
	C_{org} AR Holocene	**1.2 gC cm^{-2} ka^{-1}**	None (Currently erosional)
EARLY DIAGENETIC REGIME AND GAS SOURCE	Organic matter degradation by POCSR and ME	**high**	low
	SMT	125-162cm	**80-110cm**
	Sulphate reduction	**60% POCSR** 40% AOM	3% POCSR **97% AOM**
	Carbon source for diagentic reactions	Marine C_{org} sedimentation (from above)	Methane seepage (from below)
	Gas source	Microbial	Thermogenic (+ primary and/or secondary microbial methane)

7 Acknowledgments

We thank the captain and the crew of RV Helmer Hansen for their support during the cruise. We are also grateful to Clea Fabian and Johan Faust for support during sampling at sea. We would further like to thank the NGU laboratory (Trondheim), the Inorganic Geochemistry lab at the Center for Marine Environmental Sciences, MARUM (Bremen), Prof. Dr. Stefano Bernasconi (ETH Zürich) and Serge Robert (EAWAG) for support during geochemical analyses. The authors acknowledge funding from RWE-Dea (now DEA) (C-1648/1) and from the Norwegian Research Council through CAGE-Center for Arctic Gas Hydrate, Environment and Climate (grant 223259).

8 References

Bauer, J.E., Cai, W.-J., Raymond, P.A., Bianchi, T.S., Hopkinson, C.S., Regnier, P.A.G., 2013. The changing carbon cycle of the coastal ocean. Nature, 504(7478): 61-70.

Bellec, V., Bøe, R., Thorsnes, T., Rise, L., Dolan, M., Elvenes, S., Lepland, A., Selboskar, O.H., 2012. Geologisk Havbunnskart, Kart 6183001400. Norges geologiske undersøkelse.

Bernard, B., Brooks, J.M., Sackett, W.M., 1977. A Geochemical Model For Characterization Of Hydrocarbon Gas Sources In Marine Sediments. Offshore Technology Conference.

Bernard, B.B., Brooks, J.M., Sackett, W.M., 1978. Light hydrocarbons in recent Texas continental shelf and slope sediments. Journal of Geophysical Research: Oceans, 83(C8): 4053-4061.

Bernard, B.B., Orange, D.L., Brooks, J.M., Decker, J., 2013. Interstitial Light Hydrocarbon Gases in Jumbo Piston Cores Offshore Indonesia: Thermogenic or Biogenic?, Offchre Technology Conference 2013. Offshore Technology Conference, Houston, Texas.

Berner, R.A., 1980. Early Diagenesis. A Theoretical Approach. Princeton University Press, Princeton, N. J.

Berner, R.A., 1982. Burial of organic carbon and pyrite sulfur in the modern ocean; its geochemical and environmental significance. American Journal of Science, 282(4): 451-473.

Bianchi, T.S., Bauer, J.E., 2011. 5.03 - Particulate Organic Carbon Cycling and Transformation. In: Wolanski, E., McLusky, D. (Eds.), Treatise on Estuarine and Coastal Science. Academic Press, Waltham, pp. 69-117.

Blaauw, M., 2010. Methods and code for 'classical' age-modelling of radiocarbon sequences. Quaternary Geochronology, 5(5): 512-518.

Boetius, A., Ravenschlag, K., Schubert, C.J., Rickert, D., Widdel, F., Gieseke, A., Amann, R., Jorgensen, B.B., Witte, U., Pfannkuche, O., 2000. A marine microbial consortium apparently mediating anaerobic oxidation of methane. Nature, 407(6804): 623-626.

Boetius, A., Wenzhöfer, F., 2013. Seafloor oxygen consumption fuelled by methane from cold seeps. Nature Geosci, 6(9): 725-734.

Borowski, W.S., Paull, C.K., Ussler, W., 1996. Marine pore-water sulfate profiles indicate in situ methane flux from underlying gas hydrate. Geology, 24(7): 655-658.

Borowski, W.S., Paull, C.K., Ussler Iii, W., 1997. Carbon cycling within the upper methanogenic zone of continental rise sediments; An example from the methane-rich sediments overlying the Blake Ridge gas hydrate deposits. Marine Chemistry, 57(3–4): 299-311.

Borowski, W.S., Paull, C.K., Ussler Iii, W., 1999. Global and local variations of interstitial sulfate gradients in deep-water, continental margin sediments: Sensitivity to underlying methane and gas hydrates. Marine Geology, 159(1–4): 131-154.

Botz, R., Pokojski, H.-D., Schmitt, M., Thomm, M., 1996. Carbon isotope fractionation during bacterial methanogenesis by CO2 reduction. Organic Geochemistry, 25(3–4): 255-262.

Bøe, R., Bellec, V.K., Dolan, M.F.J., Buhl-Mortensen, P., Buhl-Mortensen, L., Slagstad, D., Rise, L., 2009. Giant sandwaves in the Hola glacial trough off Vesterålen, North Norway. Marine Geology, 267(1–2): 36-54.

Bøe, R., Skarðhamar, J., Rise, L., Dolan, M.F.J., Bellec, V.K., Winsborrow, M., Skagseth, Ø., Knies, J., King, E.L., Walderhaug, O., Chand, S., Buenz, S., Mienert, J., 2015. Sandwaves and sand transport on the Barents Sea continental slope offshore northern Norway. Marine and Petroleum Geology, 60: 34-53.

Cai, W.-J., Dai, M., Wang, Y., 2006. Air-sea exchange of carbon dioxide in ocean margins: A province-based synthesis. Geophysical Research Letters, 33(12): n/a-n/a.

Chand, S., Rise, L., Bellec, V., Dolan, M., Bøe, R., Thorsnes, T., Buhl-Mortensen, P., 2008. Active Venting System Offshore Northern Norway. Eos, Transactions American Geophysical Union, 89(29): 261-262.

Chen, C.T.A., Huang, T.H., Chen, Y.C., Bai, Y., He, X., Kang, Y., 2013. Air–sea exchanges of CO2 in the world's coastal seas. Biogeosciences, 10(10): 6509-6544.

Chung, H.M., Gormly, J.R., Squires, R.M., 1988. Origin of gaseous hydrocarbons in subsurface environments: Theoretical considerations of carbon isotope distribution. Chemical Geology, 71(1–3): 97-104.

Cline, J.D., 1969. Spectrophotometric determination of hydrogen sulfide in natural waters. Limnology and Oceanography, 14: 454 - 458.
Conrad, R., 2005. Quantification of methanogenic pathways using stable carbon isotopic signatures: a review and a proposal. Organic Geochemistry, 36(5): 739-752.
Crémière, A., Pierre, C., Blanc-Valleron, M.-M., Zitter, T., Çağatay, M.N., Henry, P., 2012. Methane-derived authigenic carbonates along the North Anatolian fault system in the Sea of Marmara (Turkey). Deep Sea Research Part I: Oceanographic Research Papers, 66: 114-130.
Crémière, A., Bayon, G., Ponzevera, E., Pierre, C., 2013. Paleo-environmental controls on cold seep carbonate authigenesis in the Sea of Marmara. Earth and Planetary Science Letters, 376(0): 200-211.
Dale, A.W., Regnier, P., Knab, N.J., Jørgensen, B.B., Van Cappellen, P., 2008. Anaerobic oxidation of methane (AOM) in marine sediments from the Skagerrak (Denmark): II. Reaction-transport modeling. Geochimica et Cosmochimica Acta, 72(12): 2880-2894.
de Haas, H., van Weering, T.C.E., de Stigter, H., 2002. Organic carbon in shelf seas: sinks or sources, processes and products. Continental Shelf Research, 22(5): 691-717.
Dearing, J.A., 1994. Environmental Magnetic Susceptibility: Using the Bartington MS2 System, Kenilworth, UK.
Dickens, G.R., Schroeder, D., Hinrichs, K.-U., Party, a.t.L.S., 2003. The pressure core sampler (PCS) on ODP Leg 201: general operations and gas release. In: D'Hondt, S.L., Jørgensen, B.B., Miller, D.J., al., e. (Eds.), Proceedings of the Ocean Drilling Program, Initial Reports, pp. 1-22.
Dimitrakopoulos, R., Muehlenbachs, K., 1987. Isotopes in the sedimentary cycleBiodegradation of petroleum as a source of 13C-enriched carbon dioxide in the formation of carbonate cement. Chemical Geology: Isotope Geoscience section, 65(3): 283-291.
Elvsborg, A., 1979. Late Quaternary sedimentation in a glacial trough on the continental shelf off Troms, northern Norway. Norsk Geologisk Tidsskrift, 59: 309-325.
Etiope, G., Feyzullayev, A., Milkov, A.V., Waseda, A., Mizobe, K., Sun, C.H., 2009. Evidence of subsurface anaerobic biodegradation of hydrocarbons and potential secondary methanogenesis in terrestrial mud volcanoes. Marine and Petroleum Geology, 26(9): 1692-1703.
Farquhar, G.D., Ehleringer, J.R., Hubick, K.T., 1989. Carbon Isotope Discrimination and Photosynthesis. Annual Review of Plant Physiology and Plant Molecular Biology, 40(1): 503-537.
Fenchel, T., King, G.M., Blackburn, T.H., 1998. Bacterial Biogeochemistry: the Ecophysiology of Mineral Cycling. Academic Press, San Diego.
Fenchel, T., King, G.M., Blackburn, T.H., 2012a. Chapter 3 - Degradation of Organic Polymers and Hydrocarbons. In: Blackburn, T., Fenchel, T., King, G.M. (Eds.), Bacterial Biogeochemistry (Third Edition). Academic Press, Boston, pp. 49-57.
Fenchel, T., King, G.M., Blackburn, T.H., 2012b. Chapter 5 - The Water Column. In: Blackburn, T., Fenchel, G.M., King, T.H. (Eds.), Bacterial Biogeochemistry (Third Edition). Academic Press, Boston, pp. 67-88.
Forwick, M., Vorren, T.O., 2009. Late Weichselian and Holocene sedimentary environments and ice rafting in Isfjorden, Spitsbergen. Palaeogeography, Palaeoclimatology, Palaeoecology, 280(1–2): 258-274.
Haeckel, M., König, I., Riech, V., Weber, M.E., Suess, E., 2001. Pore water profiles and numerical modelling of biogeochemical processes in Peru Basin deep-sea sediments. Deep Sea Research Part II: Topical Studies in Oceanography, 48(17–18): 3713-3736.
Hall, I.R., McCave, I.N., 1998. Glacial-interglacial variation in organic carbon burial on the slope of the N.W. European Continental Margin (48°–50°N). Progress in Oceanography, 42(1–4): 37-60.
Hall, P.O.J., Aller, R.C., 1992. Rapid, small-volume, flow injection analysis for C02, and NH4+ in marine and freshwaters. Limnology and Oceanography, 35: 1113-1119.
Hansen, J.W., Bakke, S., Fanavoll, S., 1992. Shallow drilling Nordland VI and VII 1991. IKU Report, 23.
Hartnett, H.E., Keil, R.G., Hedges, J.I., Devol, A.H., 1998. Influence of oxygen exposure time on organic carbon preservation in continental margin sediments. Nature, 391(6667): 572-575.

Hedges, J.I., Keil, R.G., 1995. Sedimentary organic matter preservation: an assessment and speculative synthesis. Marine Chemistry, 49(2–3): 81-115.

Henrichs, S.M., 1992. Early diagenesis of organic matter in marine sediments: progress and perplexity. Marine Chemistry, 39(1–3): 119-149.

Heuer, V.B., Pohlman, J.W., Torres, M.E., Elvert, M., Hinrichs, K.-U., 2009. The stable carbon isotope biogeochemistry of acetate and other dissolved carbon species in deep subseafloor sediments at the northern Cascadia Margin. Geochimica et Cosmochimica Acta, 73(11): 3323-3336.

Hinrichs, K.-U., Hayes, J.M., Sylva, S.P., Brewer, P.G., DeLong, E.F., 1999. Methane-consuming archaebacteria in marine sediments. Nature, 398(6730): 802-805.

Hinrichs, K.-U., Hayes, J.M., Bach, W., Spivack, A.J., Hmelo, L.R., Holm, N.G., Johnson, C.G., Sylva, S.P., 2006. Biological formation of ethane and propane in the deep marine subsurface. Proceedings of the National Academy of Sciences, 103(40): 14684-14689.

Holler, T., Wegener, G., Knittel, K., Boetius, A., Brunner, B., Kuypers, M.M.M., Widdel, F., 2009. Substantial 13C/12C and D/H fractionation during anaerobic oxidation of methane by marine consortia enriched in vitro. Environmental Microbiology Reports, 1(5): 370-376.

Hong, W.-L., Torres, M., Kim, J.-H., Choi, J., Bahk, J.-J., 2013. Carbon cycling within the sulfate-methane-transition-zone in marine sediments from the Ulleung Basin. Biogeochemistry, 115(1-3): 129-148.

Hong, W.-L., Solomon, E.A., Torres, M.E., 2014a. A kinetic-model approach to quantify the effect of mass transport deposits on pore water profiles in the Krishna–Godavari Basin, Bay of Bengal. Marine and Petroleum Geology, 58, Part A: 223-232.

Hong, W.-L., Torres, M.E., Kim, J.-H., Choi, J., Bahk, J.-J., 2014b. Towards quantifying the reaction network around the sulfate–methane-transition-zone in the Ulleung Basin, East Sea, with a kinetic modeling approach. Geochimica et Cosmochimica Acta, 140: 127-141.

Hong, W.-L., Sauer, S., Panieri, G., Ambrose Jr., W., James, R.H., Plaza-Faverola, A., Schneider, A., accepted. Removal of methane through hydrological, microbial, and geochemical processes in the shallow sediments of pockmarks along eastern Vestnesa Ridge (Svalbard). Limnology and Oceanography.

Hounslow, M.W., Maher, B.A., 1999. Source of the climate signal recorded by magnetic susceptibility variations in Indian Ocean sediments. Journal of Geophysical Research: Solid Earth, 104(B3): 5047-5061.

Hovland, M., Judd, A.G., 1988. Seabed Pockmarks and Seepages. Impact on Geology, Biology and Marine Environment. Graham & Trotman London, Dordrecht, Boston, 293 pp.

Jin, Q., Bethke, C.M., 2005. Predicting the rate of microbial respiration in geochemical environments. Geochimica et Cosmochimica Acta, 69(5): 1133-1143.

Johnson, M.A., Kenyon, N.H., Belderson, R.H., Stride, A.H., 1982. Sand transport. In: Stride, A.H. (Ed.), Offshore Tidal Sands. Springer Netherlands, pp. 58-94.

Jones, D.M., Head, I.M., Gray, N.D., Adams, J.J., Rowan, A.K., Aitken, C.M., Bennett, B., Huang, H., Brown, A., Bowler, B.F.J., Oldenburg, T., Erdmann, M., Larter, S.R., 2008. Crude-oil biodegradation via methanogenesis in subsurface petroleum reservoirs. Nature, 451(7175): 176-180.

Katz, B.J., Narimanov, A., Huseinzadeh, R., 2002. Significance of microbial processes in gases of the South Caspian basin. Marine and Petroleum Geology, 19(6): 783-796.

Katz, B.J., 2011. Microbial Processes and Natural Gas Accumulations. The Open Geology Journal, 5: 75-83.

Keil, R., 2015. Carbon cycle: Hoard of fjord carbon. Nature Geosci, 8(6): 426-427.

Knies, J., Hald, M., Ebbesen, H., Mann, U., Vogt, C., 2003. A deglacial–middle Holocene record of biogenic sedimentation and paleoproductivity changes from the northern Norwegian continental shelf. Paleoceanography, 18(4): n/a-n/a.

Knies, J., Martinez, P., 2009. Organic matter sedimentation in the western Barents Sea region: Terrestrial and marine contribution based on isotopic composition and organic nitrogen content. Norwegian Journal of Geology / Norsk Geologisk Forening, 89(1/2): 79-89.

Laberg, J.S., Stoker, M.S., Dahlgren, K.I.T., Haas, H.d., Haflidason, H., Hjelstuen, B.O., Nielsen, T., Shannon, P.M., Vorren, T.O., van Weering, T.C.E., Ceramicola, S., 2005. Cenozoic alongslope processes and sedimentation on the NW European Atlantic margin. Marine and Petroleum Geology, 22(9–10): 1069-1088.

Laruelle, G.G., Dürr, H.H., Slomp, C.P., Borges, A.V., 2010. Evaluation of sinks and sources of CO2 in the global coastal ocean using a spatially-explicit typology of estuaries and continental shelves. Geophysical Research Letters, 37(15): n/a-n/a.

Lehmann, M.F., Bernasconi, S.M., Barbieri, A., McKenzie, J.A., 2002. Preservation of organic matter and alteration of its carbon and nitrogen isotope composition during simulated and in situ early sedimentary diagenesis. Geochimica et Cosmochimica Acta, 66(20): 3573-3584.

Li, Y.-H., Gregory, S., 1974. Diffusion of ions in sea water and in deep-sea sediments. Geochimica et Cosmochimica Acta, 38(5): 703-714.

Meyers, P.A., 1994. Preservation of elemental and isotopic source identification of sedimentary organic matter. Chemical Geology, 114(3): 289-302.

Milkov, A.V., 2010. Methanogenic biodegradation of petroleum in the West Siberian Basin (Russia): Significance for formation of giant Cenomanian gas pools. AAPG Bulletin, 94(10): 1485-1541.

Milkov, A.V., 2011. Worldwide distribution and significance of secondary microbial methane formed during petroleum biodegradation in conventional reservoirs. Organic Geochemistry, 42(2): 184-207.

Murphy, J., Riley, J.P., 1962. A modified single solution method for the determination of phosphate in natural waters. Analytica Chimica Acta, 27(0): 31-36.

Müller, P.J., Suess, E., 1979. Productivity, sedimentation rate, and sedimentary organic matter in the oceans—I. Organic carbon preservation. Deep Sea Research Part A. Oceanographic Research Papers, 26(12): 1347-1362.

Nakagawa, F., Tsunogai, U., Yoshida, N., Adams, D.D., 2003. 8 - Stable isotopic compositions of bacterial light hydrocarbons in marginal marine sediments. In: Taniguchi, M.T.W.G., Wang, K., Gamo, T. (Eds.), Land and Marine Hydrogeology. Elsevier, Amsterdam, pp. 141-150.

Nauhaus, K., Boetius, A., Krüger, M., Widdel, F., 2002. In vitro demonstration of anaerobic oxidation of methane coupled to sulphate reduction in sediment from a marine gas hydrate area. Environmental Microbiology, 4(5): 296-305.

Nowaczyk, N.R., 2002. Logging of Magnetic Susceptibility. In: Last, W.M., Smol, J.P. (Eds.), Tracking Environmental Change Using Lake Sediments. Kluwer Academic Publisher, Dordrecht, The Netherlands.

Oremland, R.S., Whiticar, M.J., Strohmaier, F.E., Kiene, R.P., 1988. Bacterial ethane formation from reduced, ethylated sulfur compounds in anoxic sediments. Geochimica et Cosmochimica Acta, 52(7): 1895-1904.

Pallaser, R.J., 2000. Recognising biodegradation in gas/oil accumulations through the [dgr]13C composition of gas components. Org. Geochem., 31: 1363-1373.

Plassen, L., Vorren, T.O., 2003a. Sedimentary processes and the environment during deglaciation of a fjord basin in Ullsfjorden, North Norway. Norwegian Journal of Geology, 83: 23-26.

Plassen, L., Vorren, T.O., 2003b. Fluid flow features in fjord-fill deposits, Ullsfjorden, North Norway. Norwegian Journal of Geology, 83: 37-42.

Pohlman, J.W., Canuel, E.A., Chapman, N.R., Spence, G.D., Whiticar, M.J., Coffin, R.B., 2005. The origin of thermogenic gas hydrates on the northern Cascadia Margin as inferred from isotopic (13C/12C and D/H) and molecular composition of hydrate and vent gas. Organic Geochemistry, 36(5): 703-716.

Pohlman, J.W., Riedel, M., Bauer, J.E., Canuel, E.A., Paull, C.K., Lapham, L., Grabowski, K.S., Coffin, R.B., Spence, G.D., 2013. Anaerobic methane oxidation in low-organic content methane seep sediments. Geochimica et Cosmochimica Acta, 108(0): 184-201.

Presley, B.J., Kaplan, I.R., 1968. Changes in dissolved sulfate, calcium and carbonate from interstitial water of near-shore sediments. Geochimica et Cosmochimica Acta, 32(10): 1037-1048.

Rau, G.H., Sweeney, R.E., Kaplan, I.R., 1982. Plankton 13C: 12C ratio changes with latitude: differences between northern and southern oceans. Deep Sea Research Part A. Oceanographic Research Papers, 29(8): 1035-1039.

Reeburgh, W.S., 2007. Oceanic Methane Biogeochemistry. Chemical Reviews, 107(2): 486-513.

Reimer, P.J., Bard, E., Bayliss, A., Beck, J.W., Blackwell, P.G., Bronk Ramsey, C., Buck, C.E., Cheng, H., Edwards, R.L., Friedrich, M., Grootes, P.M., Guilderson, T.P., Haflidason, H., Hajdas, I., Hatté, C., Heaton, T.J., Hoffmann, D.L., Hogg, A.G., Hughen, K.A., Kaiser, K.F., Kromer, B., Manning, S.W., Niu, M., Reimer, R.W., Richards, D.A., Scott, E.M., Southon, J.R., Staff, R.A., Turney, C.S.M., van der Plicht, J., 2013. IntCal13 and Marine13 Radiocarbon Age Calibration Curves 0–50,000 Years cal BP. Radiocarbon, 55(4): 1869-1887.

Sauer, S., Knies, J., Lepland, A., Chand, S., Eichinger, F., Schubert, C.J., 2015. Hydrocarbon sources of cold seeps off the Vesterålen coast, northern Norway. Chemical Geology, 417: 371-382.

Schubert, C.J., Calvert, S.E., 2001. Nitrogen and carbon isotopic composition of marine and terrestrial organic matter in Arctic Ocean sediments:: implications for nutrient utilization and organic matter composition. Deep Sea Research Part I: Oceanographic Research Papers, 48(3): 789-810.

Seeberg-Elverfeldt, J., Schlüter, M., Feseker, T., Kölling, M., 2005. Rhizon sampling of porewaters near the sediment-water interface of aquatic systems. Limnology and Oceanography: Methods, 3(8): 361-371.

Smelror, M., Mørk, A., Mørk, M.B.E., Weiss, H.M., Løseth, H., 2001. Middle jurassic-lower cretaceous transgressive-regressive sequences and facies distribution off northern nordland and troms, Norway. In: Ole, J.M., Tom, D. (Eds.), Norwegian Petroleum Society Special Publications: Sedimentary Environments Offshore Norway — Palaeozoic to Recent. Elsevier, pp. 211-232.

Smith, R.W., Bianchi, T.S., Allison, M., Savage, C., Galy, V., 2015. High rates of organic carbon burial in fjord sediments globally. Nature Geosci, advance online publication.

Sommer, S., Pfannkuche, O., Linke, P., Luff, R., Greinert, J., Drews, M., Gubsch, S., Pieper, M., Poser, M., Viergutz, T., 2006. Efficiency of the benthic filter: Biological control of the emission of dissolved methane from sediments containing shallow gas hydrates at Hydrate Ridge. Global Biogeochemical Cycles, 20(2): n/a-n/a.

St-Onge, G., Hillaire-Marcel, C., 2001. Isotopic constraints of sedimentary inputs and organic carbon burial rates in the Saguenay Fjord, Quebec. Marine Geology, 176(1–4): 1-22.

Steefel, C.I., 2009. CrunchFlow- Software for Modeling Multicomponent Reactive Flow and Transport.

Steefel, C.I., Druhan, J.L., Maher, K., 2014. Modeling Coupled Chemical and Isotopic Equilibration Rates. Procedia Earth and Planetary Science, 10: 208-217.

Steefel, C.I., Appelo, C.A.J., Arora, B., Jacques, D., Kalbacher, T., Kolditz, O., Lagneau, V., Lichtner, P.C., Mayer, K.U., Meeussen, J.C.L., Molins, S., Moulton, D., Shao, H., Šimůnek, J., Spycher, N., Yabusaki, S.B., Yeh, G.T., 2015. Reactive transport codes for subsurface environmental simulation. Computational Geosciences, 19(3): 445-478.

Teeri, J.A., Stowe, L.G., 1976. Climatic patterns and the distribution of C4 grasses in North America. Oecologia, 23(1): 1-12.

Tyson, R.V., 1995. Sedimentary organic matter: Organic facies and palynofacies. Chapman and Hall, London.

Vandré, C., Cramer, B., Gerling, P., Winsemann, J., 2007. Natural gas formation in the western Nile delta (Eastern Mediterranean): Thermogenic versus microbial. Organic Geochemistry, 38(4): 523-539.

Vavilin, V., 2013. Estimating changes of isotopic fractionation based on chemical kinetics and microbial dynamics during anaerobic methane oxidation: apparent zero-and first-order kinetics at high and low initial methane concentrations. Antonie van Leeuwenhoek, 103(2): 375-383.

Vorren, T.O., Hald, M., Thomsen, E., 1984. Quaternary sediments and environments on the continental shelf off northern Norway. Marine Geology, 57(1–4): 229-257.

Vorren, T.O., Lebesbye, E., Andreassen, K., Larsen, K.B., 1989. Glacigenic sediments on a passive continental margin as exemplified by the Barents Sea. Marine Geology, 85(2–4): 251-272.

Vorren, T.O., Plassen, L.I.V., 2002. Deglaciation and palaeoclimate of the Andfjord-Vågsfjord area, North Norway. Boreas, 31(2): 97-125.

Vorren, T.O., Rydningen, T.A., Baeten, N.J., Laberg, J.S., 2015. Chronology and extent of the Lofoten–Vesterålen sector of the Scandinavian Ice Sheet from 26 to 16 cal. ka BP. Boreas: Advance online publication.

Wallmann, K., Aloisi, G., Haeckel, M., Obzhirov, A., Pavlova, G., Tishchenko, P., 2006. Kinetics of organic matter degradation, microbial methane generation, and gas hydrate formation in anoxic marine sediments. Geochimica et Cosmochimica Acta, 70(15): 3905-3927.

Weber, M.E., Niessen, F., Kuhn, G., Wiedicke, M., 1997. Calibration and application of marine sedimentary physical properties using a multi-sensor core logger. Marine Geology, 136(3–4): 151-172.

Wegener, G., Boetius, A., 2009. An experimental study on short-term changes in the anaerobic oxidation of methane in response to varying methane and sulfate fluxes. Biogeosciences, 6(5): 867-876.

Whiticar, M.J., Faber, E., Schoell, M., 1986. Biogenic methane formation in marine and freshwater environments: CO2 reduction vs. acetate fermentation—Isotope evidence. Geochimica et Cosmochimica Acta, 50(5): 693-709.

Whiticar, M.J., 1999. Carbon and hydrogen isotope systematics of bacterial formation and oxidation of methane. Chemical Geology, 161(1–3): 291-314.

Winkelmann, D., Knies, J., 2005. Recent distribution and accumulation of organic carbon on the continental margin west off Spitsbergen. Geochemistry, Geophysics, Geosystems, 6(9): n/a-n/a.

Wollast, R., 1991. The coastal organic carbon cycle: fluxes, sources and sinks. In: Mantoura, R.F.C., Martin, J.-M., Wollast, R. (Eds.), Ocean Margin Processes in Global Change, Dahlem Workshop Reports. Wiley Interscience, Chichester, pp. 365–381.

Yoshinaga, M.Y., Lazar, C.S., Elvert, M., Lin, Y.-S., Zhu, C., Heuer, V.B., Teske, A., Hinrichs, K.-U., 2015. Possible roles of uncultured archaea in carbon cycling in methane-seep sediments. Geochimica et Cosmochimica Acta, 164: 35-52.

Yu, F., Zong, Y., Lloyd, J.M., Huang, G., Leng, M.J., Kendrick, C., Lamb, A.L., Yim, W.W.S., 2010. Bulk organic δ13C and C/N as indicators for sediment sources in the Pearl River delta and estuary, southern China. Estuarine, Coastal and Shelf Science, 87(4): 618-630.

Zhang, S., Yang, L., DePaolo, D.J., Steefel, C.I., 2015. Chemical affinity and pH effects on chlorite dissolution kinetics under geological CO2 sequestration related conditions. Chemical Geology, 396: 208-217.

9 Supplementary materials

9.1 The biogeochemistry network

Organic matter is consumed by sulphate (particulate organic carbon sulphate reduction, POCSR) upon burial through microbial activities. Decomposition of organic matter by POCSR consumes sulphate and releases nutrients (*e.g.,* ammonium and phosphate) following the reaction:

$$(CH_2O)(NH_3)_{\frac{N}{C}}(H_3PO_4)_{\frac{P}{C}} + 0.5SO_4^{2-} \rightarrow 0.5HS^- + aH^{12}CO_3^{2-} + bH^{13}CO_3^{2-} + (\frac{N}{C})NH_4^+ + (\frac{P}{C})HPO_4^{2-} + c^{12}CO_2 + d^{13}CO_2 + eH_2O \quad (1)$$

We explicitly included both isotopologues of DIC to account for the resulting carbon isotopic signal of the product. The stoichiometry in Eq. (1) is determined by the carbon isotopic signature and C:N:P ratios of the organic matter at both stations (Table S1). The POCSR rate was formulated as *Monod-type* rate expression with one *Monod* term:

$$R_{POCSR} = A_m k_m \exp[\frac{-Ea}{RT}]\prod a_i^n[1-\frac{Q}{K_{eq}}] \quad (2)$$

$$k_m = k_{\max}^{POCSR}\left(\frac{C_{SO4}}{C_{SO4}+K_{half}}\right) \quad (3)$$

where A_m (=1) and k_m are the surface area and kinetic constant. *Ea*, *R*, and *T* are the activation energy, ideal gas constant, and temperature. Πa_i^n is the activity product of solutes in the reaction

with their stoichiometry (*n*) as exponents. $\frac{Q}{K_{eq}}$ determines the direction of reaction where *Q* is the ion activity product and K_{eq} is the equilibrium constant. As POCSR is a kinetic-driven reaction, we arbitrarily assigned a K_{eq} to ensure the reaction always in a forward direction. $k_{\max}^{POCSR}$ is the theoretical maximum rate that was obtained by fitting the observed pore water ammonium and phosphate profiles at both sites (Table S1). K_{half} is the half saturation constant ($=100\ \mu M$; (Wegener and Boetius, 2009)), and C_{SO4} is the concentration of sulphate.

Below the depth of the sulphate reduction zone, organic matter is decomposed by methanogenesis (ME):

$$(CH_2O)(NH_3)_{\frac{N}{C}}(H_3PO_4)_{\frac{P}{C}} + fH2O \rightarrow g^{12}CH_4 + h^{13}CH_4 + iH^{12}CO_3^{2-} + jH^{13}CO_3^{2-}$$

$$k^{12}CO_2 + l^{13}CO_2 + (\frac{N}{C})NH_4^{+} + (\frac{P}{C})HPO_4^{2-} \quad (4)$$

ME is formulated as a *Monod-type* reaction (as in Eq.(2)) with three inhibition terms (Wallmann et al., 2006):

$$k_m = k_{\max}^{ME}\left(\frac{C_{SO4}+K_{in.SO4}}{K_{in.SO4}}\right)\left(\frac{C_{HCO3}+K_{in.HCO3}}{K_{in.HCO3}}\right)\left(\frac{C_{CH4}+K_{in.CH4}}{K_{in.CH4}}\right) \quad (5)$$

where $K_{in.SO4}$, $K_{in.HCO3}$, and $K_{in.CH4}$, the inhibition constants, are 1.6 mM, 15 mM and 15 mM (Wallmann et al., 2006), respectively. These inhibition terms suppress the reaction when the concentrations of sulphate and metabolic products (*i.e.*, DIC and methane) are over the threshold.

A significant fraction of the dissolved sulphate is consumed at the SMT through anaerobic oxidation of methane (AOM):

$$CH_{4(aq)} + SO_4^{2-} \rightarrow HCO_3^{-} + HS^{-} + H_2O \quad (6)$$

To account for the associated isotopic fractionation, we formulated AOM for ^{12}C and ^{13}C, individually,

as *Monod-type* reactions with two *Monod* terms:

$$^{12/13}R_{AOM} = {}^{12/13}k_{\max}^{AOM}\left(\frac{C_{SO_4}}{C_{SO_4}+K_{half-SO_4}}\right)\left(\frac{C_{^{12/13}CH_4}}{C_{^{12/13}CH_4}+{}^{12/13}K_{half-CH_4}}\right)\left(1-\frac{Q}{K_{eq}}\right) \quad (7)$$

where *C* is the concentration of electron donors or acceptors and *Q* is the ion activity product. The fractionation factor for AOM, α_{AOM}, depends on the maximum rate ($^{12/13}k_{\max}^{AOM}$) and the half saturation constant for methane ($^{12/13}K_{half-CH_4}$):

$$\alpha_{AOM} = \frac{^{12}k_{\max}^{AOM} \bullet {}^{13}K_{half-CH_4}}{^{13}k_{\max}^{AOM} \bullet {}^{12}K_{half-CH_4}} \quad (8)$$

$K_{half-SO_4}$ and $^{12}K_{half-CH_4}$ were set to be 500 µM (Wegener and Boetius, 2009) and 5 mM (Nauhaus et al., 2002; Vavilin, 2013), respectively. $^{12}k_{\max}^{AOM}$, $^{13}k_{\max}^{AOM}$ and $^{13}K_{half-CH_4}$ were obtained from fitting curves to our data and reported in Table S1. We assumed a constant α_{AOM} of 1.01 (Whiticar, 1999; Holler et al., 2009) for both cores.

A small fraction of DIC is consumed through CO_2 reduction (Borowski et al., 1997; Dale et al., 2008; Hong et al., 2013; Hong et al., 2014b), an important reaction to achieve isotopic mass balance of carbon between DIC and methane pools (Hong et al., 2013):

$$H^{12/13}CO_3^- + H^+ + 4H_{2(aq)} \rightarrow {}^{12/13}\mathrm{CH}_{4(aq)} + 3\mathrm{H_2O} \quad (9)$$

CR, one for each isotopologues of carbon, was formulated in a similar fashion as AOM with one additional inhibition term of sulphate:

$$^{12/13}R_{CR} = {}^{12/13}k_{\max}^{CR}\left(\frac{C_{H_2}}{C_{H_2}+K_{half-H_2}}\right)\left(\frac{C_{^{12/13}HCO_3}}{C_{^{12/13}HCO_3}+{}^{12/13}K_{half-HCO_3}}\right)\left(\frac{K_{in-SO_4}+C_{SO_4}}{K_{in-SO_4}}\right)\left(1-\frac{Q}{K_{eq}}\right) \quad (10)$$

A K_{half-H_2} value of 1 µM was used (Jin and Bethke, 2005). The other kinetic parameters were

obtained by fitting the profiles. The isotopic fractionation of CR (α_{CR}) was formulated as:

$$\alpha_{CR} = \frac{^{12}k_{\max}^{CR} \bullet {}^{13}K_{half-HCO_3^-}}{^{13}k_{\max}^{CR} \bullet {}^{12}K_{half-HCO_3^-}} \quad (11)$$

A constant value 1.098 was used at all sites (Whiticar, 1999; Holler et al., 2009).

To correctly account for the change of pH and alkalinity in the dissolved phase, we also included different speciation of dissolved carbonate, ammonium, and phosphate. Dissolution of CO_2 and CH_4 gases were also included although the model was set to be always water saturated (*i.e.,* no gas phase and transport). The full list of these secondary reactions and their respective equilibrium constant is included in Hong et al. (2014a).

Table S1: Model parameters

	GC 51$_{shelf}$	**GC 36$_{fjord}$**
Column length	2.89 m	3.74 m
C/N	12	7
C/P	112	120
Bottom age	18 ka	4.04 ka
$\delta^{13}C_{POC}$	-24.5‰	-21‰
$\delta^{13}C_{DIC}$ ***(ME)***	12‰	10‰
$\delta^{13}C_{CH4}$ ***(ME)***	-50‰	-90‰
$\delta^{13}C_{Calcite}$	-40‰	-40‰
a	0.559341	0.619379
b	0.006131	0.006814
c	0.429816	0.369739
d	0.004712	0.004068
e	0.434527	0.373807
f	0.065473	0.126193
g	0.494719	0.494939
h	0.005281	0.005061
i	0.064731	0.124777
j	0.000736	0.001416
k	0.429641	0.369612
l	0.004886	0.004195
$k_{\max}^{POCSR}$	10^{-9}	10^{-8}
$k_{\max}^{ME}$	$10^{-8.5}$	$10^{-8.5}$
$^{12}k_{\max}^{AOM}$	1.1E-2	1.1E-2

$^{13}k_{\max}^{AOM}$	1.3287E-4	1.3069E-4
$^{12}K_{half-CH_4}$	5E-3	5E-3
$^{13}K_{half-CH_4}$	6.1E-5	6E-5
$^{12}k_{\max}^{CR}$	1E-3	1E-3
$^{13}k_{\max}^{CR}$	3.87E-5	1.366E-5
$^{12}K_{half-HCO_3}$	1E-2	1E-2
$^{13}K_{half-HCO_3}$	4.25E-4	1.5E-4
k_m^{Ca}	$10^{-6.6}$	$10^{-7.4}$
k_m^{Mg}	$10^{-7.8}$	$10^{-8.7}$
k_m^{Pyrite}	$10^{-14.8}$	$10^{-14.8}$

9.2 Other model parameters

We used core-top and bottom pore water compositions for boundary conditions. For methane, we adjusted its concentration at the bottom of our model domain (Table S2) until the depth of the modelled SMTZ matches the observed depth. The model was initiated with the observed core-top pore water composition at each site (Table S2).

Table S2: Boundary and initial conditions

	Top boundary & Initial condition (GC 36$_{fjord}$ / GC 51$_{shelf}$)	**Bottom boundary condition** (GC 36$_{fjord}$ / GC 51$_{shelf}$)
HCO_3^-	2.2 / 2.2 mM	55 / 55 mM
$\delta^{13}C_{DIC}$	0 / 0 ‰	-1.69 / 18.9 ‰
CH_4	~0 / ~0 mM	10 / 30 mM
$\delta^{13}C_{CH4}$	-60 / -60 ‰	-89.6 / -53.7 ‰
NH_4^+	6 / 6 µM	7.6 / 0.227 mM
PO_4^{3-}	0.66 / 0.66 µM	0.3 / 0.0538 mM
SO_4^{2-}	28.3 / 28.3 mM	0 / 0 mM
HS^-	~0 / ~0 mM	1.97 / 0 mM

The depth discretization is 1 cm. A total 289 and 374 cells were simulated. Bottom ages of 18 and 4.04 ka for stations GC 51_{shelf} and GC 36_{fjord}, respectively, were used. Porosity was assumed to be constant (0.8) for both stations. The 25 ^{o}C diffusion coefficients for all pore water species are from Berner (1980) and Li and Gregory (1974). Diffusion coefficients were corrected for temperature, porosity and tortuosity to account for the slower diffusion in porous media under cold bottom water temperature (6^{o}C). CrunchFlow requires input of a cementation exponent to account for the tortuous flow in the porous media. As there is no information such as tortuosity or formation factor available, we estimated the cementation exponent from a general relationship between porosity and formation factor reported by (Berner, 1980). Dependence of temperature is accounted for by assigning the activation energy in CrunchFlow. We fit the 0 ^{o}C and 25 ^{o}C measurements by Li and Gregory (1974) and obtained a value 5.6×10^{-25} kcal/mol for this activation energy input.

9.3 References

Berner, R.A., 1980. Early Diagenesis. A Theoretical Approach. Princeton University Press, Princeton, N. J.

Borowski, W.S., Paull, C.K., Ussler Iii, W., 1997. Carbon cycling within the upper methanogenic zone of continental rise sediments; An example from the methane-rich sediments overlying the Blake Ridge gas hydrate deposits. Marine Chemistry, 57(3–4): 299-311.

Dale, A.W., Regnier, P., Knab, N.J., Jørgensen, B.B., Van Cappellen, P., 2008. Anaerobic oxidation of methane (AOM) in marine sediments from the Skagerrak (Denmark): II. Reaction-transport modeling. Geochimica et Cosmochimica Acta, 72(12): 2880-2894.

Holler, T. et al., 2009. Substantial 13C/12C and D/H fractionation during anaerobic oxidation of methane by marine consortia enriched in vitro. Environmental Microbiology Reports, 1(5): 370-376.

Hong, W.-L., Torres, M., Kim, J.-H., Choi, J., Bahk, J.-J., 2013. Carbon cycling within the sulfate-methane-transition-zone in marine sediments from the Ulleung Basin. Biogeochemistry, 115(1-3): 129-148.

Hong, W.-L., Torres, M.E., Kim, J.-H., Choi, J., Bahk, J.-J., 2014. Towards quantifying the reaction network around the sulfate–methane-transition-zone in the Ulleung Basin, East Sea, with a kinetic modeling approach. Geochimica et Cosmochimica Acta, 140: 127-141.

Jin, Q., Bethke, C.M., 2005. Predicting the rate of microbial respiration in geochemical environments. Geochimica et Cosmochimica Acta, 69(5): 1133-1143.

Li, Y.-H., Gregory, S., 1974. Diffusion of ions in sea water and in deep-sea sediments. Geochimica et Cosmochimica Acta, 38(5): 703-714.

Nauhaus, K., Boetius, A., Krüger, M., Widdel, F., 2002. In vitro demonstration of anaerobic oxidation of methane coupled to sulphate reduction in sediment from a marine gas hydrate area. Environmental Microbiology, 4(5): 296-305.

Vavilin, V., 2013. Estimating changes of isotopic fractionation based on chemical kinetics and microbial dynamics during anaerobic methane oxidation: apparent zero-and first-order kinetics at high and low initial methane concentrations. Antonie van Leeuwenhoek, 103(2): 375-383.

Wallmann, K. et al., 2006. Kinetics of organic matter degradation, microbial methane generation, and gas hydrate formation in anoxic marine sediments. Geochimica et Cosmochimica Acta, 70(15): 3905-3927.

Wegener, G., Boetius, A., 2009. An experimental study on short-term changes in the anaerobic oxidation of methane in response to varying methane and sulfate fluxes. Biogeosciences, 6(5): 867-876.

Whiticar, M.J., 1999. Carbon and hydrogen isotope systematics of bacterial formation and oxidation of methane. Chemical Geology, 161(1–3): 291-314.

10 Data

Table 7: Wet bulk density and magnetic susceptibility data of core GC 51

GC 51	Depth (cm)	Density (g/cm^3)	Depth (cm)	Mag Sus SI x 10^{-5}	Depth (cm)	Density (g/cm^3)	Depth (cm)	Mag Sus SI x 10^{-5}	Depth (cm)	Density (g/cm^3)	Depth (cm)	Mag Sus SI x 10^{-5}	Depth (cm)	Density (g/cm^3)	Depth (cm)	Mag Sus SI x 10^{-5}
					45.6	2.0	45	90	92.2	1.7	90.5	37	137.7	1.8	136	25
					46.1	1.9	45.5	103	92.7	1.8	91	30	138.2	1.8	136.5	27
	1.1	2.1	0.5	209	46.6	1.9	46	102	93.2	1.8	91.5	37	138.7	2.0	137	24
	1.6	2.1	1	296	47.1	1.9	46.5	102	93.7	1.8	92	39	139.2	2.0	137.5	30
	2.1	2.0	1.5	777	47.6	1.9	47	108	94.2	1.8	92.5	43	139.7	1.9	138	39
	2.6	2.0	2	1211	48.1	1.9	47.5	121	94.7	1.9	93	55	140.2	1.9	138.5	30
	3.1	2.0	2.5	1182	48.6	1.8	48	68	95.2	1.9	93.5	62	140.7	1.8	139	31
	3.6	2.0	3	985	49.1	1.8	48.5	65	95.7	1.9	94	49	141.2	1.8	139.5	27
	4.1	2.0	3.5	865	49.6	1.8	49	63	96.2	1.9	94.5	43	141.7	1.8	140	25
	4.6	2.0	4	543	50.1	1.8	49.5	49	96.7	1.8	95	50	142.2	1.8	140.5	25
	5.1	2.0	4.5	254	50.6	1.8	50	49	97.2	1.8	95.5	73	142.7	1.8	141	23
	5.6	2.0	5	197	51.1	1.8	50.5	58	97.7	1.8	96	43	143.2	1.8	141.5	23
	6.1	2.0	5.5	227	51.6	1.8	51	68	98.2	1.8	96.5	37	143.7	1.8	142	25
	6.6	2.0	6	169	52.1	1.8	51.5	69	98.7	1.9	97	42	144.2	1.8	142.5	32
	7.1	2.0	6.5	188	52.6	1.9	52	61	99.2	1.8	97.5	46	144.7	1.8	143	29
	7.6	1.9	7	176	53.1	1.9	52.5	61	99.7	1.8	98	53	145.2	1.8	143.5	29
	8.1	1.9	7.5	188	53.6	1.8	53	76	100.2	1.8	98.5	36	145.7	1.8	144	28
	8.6	1.9	8	283	54.1	1.8	53.5	76	100.7	1.8	99	36	146.2	1.9	144.5	24
	9.1	2.0	8.5	235	54.6	1.8	54	67	101.2	1.8	99.5	33	146.7	1.9	145	23
	9.6	2.0	9	238	55.1	1.8	54.5	63	101.7	1.8	100	39	147.2	1.8	145.5	27
	10.1	2.0	9.5	237	55.6	1.8	55	59	102.2	1.8	100.5	29	147.7	1.8	146	30
	10.6	2.0	10	138	56.1	1.8	55.5	67	102.7	1.8	101	27	148.2	1.8	146.5	32
	11.1	2.0	10.5	153	56.6	1.8	56	69	103.2	1.7	101.5	33	148.7	1.8	147	31
	11.6	2.0	11	158	57.1	1.8	56.5	53	103.7	1.8	102	28	149.2	1.8	147.5	28
	12.1	2.0	11.5	149	57.6	1.9	57	51	104.2	1.8	102.5	25	149.7	1.8	148	26
	12.6	2.0	12	196	58.1	1.8	57.5	45	104.7	1.8	103	26	150.2	1.8	148.5	25
	13.1	1.9	12.5	172	58.6	1.8	58	46	105.2	1.8	103.5	29	150.7	1.8	149	24
	13.6	2.0	13	125	59.1	1.8	58.5	43	105.7	1.8	104	28	151.2	1.8	149.5	28
	14.1	2.0	13.5	155	59.6	1.8	59	51	106.2	1.8	104.5	34	151.7	1.7	150	27
	14.6	2.0	14	130	60.1	1.8	59.5	51	106.7	1.8	105	32	152.2	1.7	150.5	28
	15.1	2.0	14.5	102	60.6	1.8	60	49	107.2	1.8	105.5	31	152.7	1.8	151	25
	15.6	2.0	15	76	61.1	1.8	60.5	50	107.7	1.8	106	28	153.2	1.8	151.5	22
	16.1	2.0	15.5	60	61.6	1.8	61	48	108.2	1.8	106.5	28	153.7	1.8	152	22
	16.6	2.0	16	55	62.1	1.8	61.5	46	108.7	1.8	107	28	154.2	1.8	152.5	22
	17.1	2.0	16.5	51	62.6	1.9	62	58	109.2	1.8	107.5	27	154.7	1.8	153	24
	17.6	2.0	17	105	63.1	1.9	62.5	64	109.7	1.8	108	38	155.2	1.8	153.5	26
	18.1	2.0	17.5	78	63.6	1.9	63	85	110.2	1.8	108.5	49	155.7	1.8	154	34
	18.6	2.0	18	69	64.1	1.8	63.5	101	110.7	1.8	109	29	156.2	1.9	154.5	36
	19.1	2.0	18.5	54	64.6	1.8	64	121	111.2	1.8	109.5	39	156.7	1.9	155	29
	19.6	2.1	19	50	65.1	1.8	64.5	104	111.7	1.7	110	230	157.2	1.8	155.5	33
	20.1	2.0	19.5	47	65.6	1.8	65	76	112.2	1.7	110.5	87	157.7	1.8	156	33
	20.6	2.0	20	43	66.1	1.8	65.5	57	112.7	1.8	111	29	158.2	1.8	156.5	32
	21.1	1.9	20.5	35	66.6	1.8	66	64	113.2	1.8	111.5	26	158.7	1.7	157	32
	21.6	2.0	21	35	67.1	1.8	66.5	64	113.7	1.8	112	29	159.2	1.8	157.5	26
	22.1	1.9	21.5	33	67.6	1.8	67	69	114.2	1.8	112.5	30	159.7	1.8	158	25
	22.6	2.0	22	36	68.1	1.8	67.5	62	114.7	1.8	113	32	160.2	1.8	158.5	24
	23.1	2.0	22.5	50	68.6	1.8	68	61	115.2	1.9	113.5	38	160.7	1.7	159	23
	23.6	2.0	23	81	69.1	1.8	68.5	56	115.7	1.8	114	36	161.2	1.8	159.5	26
	24.1	2.0	23.5	29	69.6	1.8	69	58	116.2	1.8	114.5	42	161.7	1.8	160	25
	24.6	2.0	24	22	70.1	1.8	69.5	69	116.7	1.7	115	31	162.2	1.8	160.5	27
	25.1	2.1	24.5	16	70.6	1.8	70	64	117.2	1.8	115.5	28	162.7	1.8	161	27
	25.6	2.1	25	13	71.1	1.8	70.5	56	117.7	1.8	116	26	163.2	1.8	161.5	26
	26.1	2.1	25.5	13	71.6	1.8	71	61	118.2	1.8	116.5	26	163.7	1.7	162	26
	26.6	1.9	26	11	72.1	1.8	71.5	38	118.7	1.9	117	30	164.2	1.8	162.5	29
	27.1	1.9	26.5	14	72.6	1.8	72	34	119.2	1.9	117.5	39	164.7	1.7	163	26
	27.6	2.0	27	17	73.1	1.8	72.5	26	119.7	1.9	118	41	165.2	1.7	163.5	26
	28.1	2.0	27.5	22	73.6	1.9	73	32	120.2	1.8	118.5	31	165.7	1.7	164	24
	28.6	2.0	28	31	74.1	1.9	73.5	50	120.7	1.8	119	28	166.2	1.8	164.5	22
	29.1	2.0	28.5	32	74.6	1.8	74	89	121.2	1.8	119.5	28	166.7	1.7	165	20
	29.6	2.0	29	36	75.1	1.8	74.5	64	121.7	1.9	120	29	167.2	1.7	165.5	20
	30.1	2.0	29.5	36	75.6	1.8	75	56	122.2	1.9	120.5	34	167.7	1.7	166	24
	30.6	2.0	30	51	76.1	1.8	75.5	53	122.7	1.9	121	39	168.2	1.7	166.5	26
	31.1	2.0	30.5	39	76.6	1.8	76	51	123.2	1.9	121.5	30	168.7	1.7	167	22
	31.6	2.0	31	30	77.1	1.9	76.5	60	123.7	1.8	122	36	169.2	1.7	167.5	29
	32.1	2.0	31.5	42	77.6	1.9	77	60	124.2	1.8	122.5	33	169.7	1.7	168	22
	32.6	2.0	32	79	78.1	1.8	77.5	49	124.7	1.7	123	33	170.2	1.7	168.5	20
	33.1	2.0	32.5	65	78.6	1.8	78	42	125.2	1.7	123.5	28	170.7	1.7	169	19
	33.6	2.0	33	40	79.1	1.8	78.5	42	125.7	1.8	124	29	171.2	1.8	169.5	22
	34.1	2.0	33.5	36	79.6	1.8	79	37	126.2	1.7	124.5	28	171.7	1.8	170	23
	34.6	2.0	34	56	80.1	1.9	79.5	65	126.7	1.8	125	26	172.2	1.7	170.5	23
	35.1	2.0	34.5	72	80.6	1.9	80	52	127.2	1.8	125.5	28	172.7	1.7	171	28
	35.6	2.0	35	65	81.1	1.9	80.5	64	127.7	1.8	126	29	173.2	1.7	171.5	26
	36.1	2.0	35.5	82	81.6	1.9	81	59	128.2	1.8	126.5	29	173.7	1.7	172	23
	36.6	2.0	36	77	82.1	1.9	81.5	60	128.7	1.8	127	27	174.2	1.7	172.5	21
	37.1	2.0	36.5	70	82.6	1.8	82	65	129.2	1.8	127.5	27	174.7	1.7	173	19
	37.6	2.0	37	62	83.1	1.8	82.5	77	129.7	1.8	128	27	175.2	1.7	173.5	19
	38.1	2.0	37.5	56	83.6	1.8	83	43	130.2	1.8	128.5	28	175.7	1.8	174	20
	38.6	2.0	38	59	84.1	1.9	83.5	39	130.7	1.8	129	28	176.2	1.8	174.5	22
	39.1	2.0	38.5	54	84.6	1.8	84	44	131.2	1.8	129.5	29	176.7	1.8	175	25
	39.6	2.0	39	44	85.1	1.9	84.5	45	131.7	1.9	130	30	177.2	1.8	175.5	24
	40.1	2.0	39.5	40	85.6	1.9	85	43	132.2	1.9	130.5	29	177.7	1.8	176	27
	40.6	2.0	40	39	86.1	1.9	85.5	49	132.7	1.8	131	31	178.2	1.7	176.5	24
	41.1	2.0	40.5	35	86.6	1.8	86	59	133.2	1.9	131.5	30	178.7	1.7	177	24
	41.6	2.0	41	38	87.1	1.8	86.5	44	133.7	2.0	132	28	179.2	1.7	177.5	23
	42.1	1.9	41.5	44	87.6	1.8	87	47	134.2	2.0	132.5	31	179.7	1.7	178	22
	42.6	1.9	42	51	88.1	1.8	87.5	39	134.7	1.9	133	32	180.2	1.7	178.5	24
	43.1	1.9	42.5	70	88.6	1.7	88	30	135.2	1.9	133.5	31	180.7	1.7	179	20
	43.6	2.0	43	65	89.1	1.8	88.5	27	135.7	1.9	134	30	181.2	1.7	179.5	20
	44.1	2.0	43.5	65	89.6	1.8	89	31	136.2	1.9	134.5	33	181.7	1.7	180	24
	44.6	2.0	44	67	90.1	1.8	89.5	35	136.7	1.8	135	29	182.2	1.7	180.5	25
	45.1	2.0	44.5	75	90.6	1.7	90	40	137.2	1.8	135.5	28	182.7	1.7	181	93

Table 1 continued: Wet bulk density and magnetic susceptibility data of core GC 51

Depth (cm)	Density (g/cm^3)	*Depth (cm)*	Mag Sus SI x 10^{-5}	*Depth (cm)*	Density (g/cm^3)	*Depth (cm)*	Mag Sus SI x 10^{-5}	*Depth (cm)*	Density (g/cm^3)	*Depth (cm)*	Mag Sus SI x 10^{-5}
183.2	1.7	*181.5*	35	*231*	1.6	*234*	22	*276.5*	1.6	*279.5*	18
183.7	1.7	*182*	24	*231.5*	1.6	*234.5*	22	*277*	1.6	*280*	18
184.2	1.7	*182.5*	26	*232*	1.6	*235*	22	*277.5*	1.6	*280.5*	20
184.7	1.7	*183*	26	*232.5*	1.6	*235.5*	21	*278*	1.6	*281*	19
185.2	1.7	*183.5*	24	*233*	1.6	*236*	20	*278.5*	1.6	*281.5*	19
185.7	1.6	*184*	24	*233.5*	1.6	*236.5*	20	*279*	1.5	*282*	24
186.2	1.6	*184.5*	24	*234*	1.6	*237*	20	*279.5*	1.5	*282.5*	22
186.7	1.6	*185*	24	*234.5*	1.6	*237.5*	20	*280*	1.5	*283*	24
187.2	1.7	*185.5*	21	*235*	1.6	*238*	19	*280.5*	1.5	*283.5*	31
187.7	1.7	*186*	20	*235.5*	1.6	*238.5*	19	*281*	1.5	*284*	33
188.2	1.7	*186.5*	20	*236*	1.6	*239*	19	*281.5*	1.5	*284.5*	35
188.7	1.7	*194*	22	*236.5*	1.6	*239.5*	19	*282*	1.5	*285*	44
189.2	1.7	*194.5*	23	*237*	1.6	*240*	18	*282.5*	1.4	*285.5*	46
189.7	1.6	*195*	22	*237.5*	1.6	*240.5*	19	*283*	1.4	*286*	40
190.2	1.7	*195.5*	21	*238*	1.6	*241*	19	*283.5*	1.4	*286.5*	19
190.7	1.7	*196*	21	*238.5*	1.6	*241.5*	20	*284*	1.5	*287*	4
191.2	1.7	*196.5*	21	*239*	1.6	*242*	19	*284.5*	1.5	*287.5*	1
191.7	1.7	*197*	21	*239.5*	1.6	*242.5*	17	*285*	1.6	*288*	0
194.5	1.7	*197.5*	23	*240*	1.6	*243*	17	*285.5*	1.6	*288.5*	0
195	1.6	*198*	23	*240.5*	1.6	*243.5*	17	*286*	1.5	*289*	0
195.5	1.7	*198.5*	24	*241*	1.6	*244*	18	*286.5*	1.1	*289.5*	2
196	1.7	*199*	23	*241.5*	1.6	*244.5*	19	*287*	0.6	*290*	16
196.5	1.7	*199.5*	26	*242*	1.6	*245*	19	*287.5*	0.2	*290.5*	40
197	1.7	*200*	24	*242.5*	1.6	*245.5*	19	*288*	0.0	*291*	25
197.5	1.6	*200.5*	24	*243*	1.6	*246*	19	*288.5*	-0.1	*291.5*	58
198	1.6	*201*	25	*243.5*	1.6	*246.5*	20	*289*	-0.1	*292*	47
198.5	1.7	*201.5*	21	*244*	1.6	*247*	21	*289.5*	-0.1	*292.5*	52
199	1.7	*202*	21	*244.5*	1.6	*247.5*	22	*290*	-0.2	*293*	48
199.5	1.7	*202.5*	23	*245*	1.6	*248*	22	*290.5*	0.0	*293.5*	52
200	1.7	*203*	22	*245.5*	1.6	*248.5*	27	*291*	0.4	*294*	56
200.5	1.7	*203.5*	23	*246*	1.6	*249*	27	*291.5*	1.2	*294.5*	61
201	1.7	*204*	23	*246.5*	1.6	*249.5*	31	*292*	1.4	*295*	43
201.5	1.7	*204.5*	25	*247*	1.6	*250*	33	*292.5*	1.5	*295.5*	43
202	1.7	*205*	26	*247.5*	1.6	*250.5*	34	*293*	1.5	*296*	49
202.5	1.7	*205.5*	29	*248*	1.6	*251*	34	*293.5*	1.6	*296.5*	46
203	1.7	*206*	44	*248.5*	1.6	*251.5*	36	*294*	1.8	*297*	46
203.5	1.6	*206.5*	43	*249*	1.6	*252*	34	*294.5*	1.9	*297.5*	47
204	1.7	*207*	27	*249.5*	1.6	*252.5*	30	*295*	1.9	*298*	42
204.5	1.6	*207.5*	21	*250*	1.6	*253*	32	*295.5*	1.9	*298.5*	67
205	1.6	*208*	19	*250.5*	1.6	*253.5*	33	*296*	1.8	*299*	44
205.5	1.7	*208.5*	19	*251*	1.6	*254*	34	*296.5*	1.8	*299.5*	51
206	1.7	*209*	20	*251.5*	1.6	*254.5*	28	*297*	2.0	*300*	50
206.5	1.6	*209.5*	20	*252*	1.6	*255*	27	*297.5*	2.0	*300.5*	45
207	1.6	*210*	20	*252.5*	1.6	*255.5*	28	*298*	2.0	*301*	35
207.5	1.6	*210.5*	20	*253*	1.6	*256*	30	*298.5*	2.0	*301.5*	26
208	1.6	*211*	20	*253.5*	1.6	*256.5*	26	*299*	2.1	*302*	121
208.5	1.6	*211.5*	20	*254*	1.6	*257*	26	*299.5*	2.1	*302.5*	71
209	1.6	*212*	20	*254.5*	1.6	*257.5*	26	*300*	2.1	*303*	38
209.5	1.6	*212.5*	20	*255*	1.6	*258*	31	*300.5*	2.1	*303.5*	39
210	1.6	*213*	21	*255.5*	1.6	*258.5*	37	*301*	1.9	*304*	39
210.5	1.6	*213.5*	22	*256*	1.6	*259*	35	*302.5*	2.0	*305.5*	59
211	1.7	*214*	23	*256.5*	1.6	*259.5*	32	*303*	1.9	*306*	56
211.5	1.6	*214.5*	22	*257*	1.6	*260*	30	*303.5*	1.9	*306.5*	37
212	1.6	*215*	21	*257.5*	1.6	*260.5*	32	*304*	2.0	*307*	29
212.5	1.6	*215.5*	20	*258*	1.6	*261*	27	*304.5*	2.0	*307.5*	25
213	1.7	*216*	21	*258.5*	1.6	*261.5*	31	*305*	2.0	*308*	29
213.5	1.6	*216.5*	27	*259*	1.6	*262*	26	*305.5*	2.0	*308.5*	26
214	1.7	*217*	93	*259.5*	1.6	*262.5*	26	*306*	2.0	*309*	13
214.5	1.6	*217.5*	33	*260*	1.6	*263*	31	*306.5*	2.0	*309.5*	19
215	1.6	*218*	24	*260.5*	1.6	*263.5*	30	*307*	2.0	*310*	66
215.5	1.7	*218.5*	22	*261*	1.6	*264*	34	*307.5*	2.0		
216	1.7	*219*	24	*261.5*	1.6	*264.5*	38	*308*	1.6		
216.5	1.7	*219.5*	30	*262*	1.6	*265*	57	*308.5*	0.9		
217	1.7	*220*	34	*262.5*	1.6	*265.5*	75	*309*	0.9		
217.5	1.7	*220.5*	37	*263*	1.6	*266*	85	*309.5*	1.0		
218	1.7	*221*	37	*263.5*	1.6	*266.5*	80	*310*	1.0		
218.5	1.7	*221.5*	98	*264*	1.6	*267*	82	*310.5*	1.2		
219	1.7	*222*	36	*264.5*	1.6	*267.5*	66	*311*	1.2		
219.5	1.7	*222.5*	25	*265*	1.6	*268*	61	*311.5*	1.3		
220	1.7	*223*	22	*265.5*	1.6	*268.5*	63	*312*	1.0		
220.5	1.7	*223.5*	21	*266*	1.6	*269*	70				
221	1.7	*224*	21	*266.5*	1.6	*269.5*	67				
221.5	1.7	*224.5*	21	*267*	1.7	*270*	66				
222	1.7	*225*	21	*267.5*	1.6	*270.5*	49				
222.5	1.6	*225.5*	23	*268*	1.6	*271*	49				
223	1.6	*226*	26	*268.5*	1.6	*271.5*	45				
223.5	1.6	*226.5*	21	*269*	1.6	*272*	47				
224	1.6	*227*	20	*269.5*	1.6	*272.5*	40				
224.5	1.6	*227.5*	21	*270*	1.6	*273*	44				
225	1.6	*228*	20	*270.5*	1.6	*273.5*	41				
225.5	1.6	*228.5*	21	*271*	1.6	*274*	38				
226	1.6	*229*	31	*271.5*	1.7	*274.5*	37				
226.5	1.6	*229.5*	45	*272*	1.7	*275*	41				
227	1.6	*230*	23	*272.5*	1.7	*275.5*	56				
227.5	1.6	*230.5*	21	*273*	1.8	*276*	40				
228	1.6	*231*	19	*273.5*	1.8	*276.5*	31				
228.5	1.6	*231.5*	19	*274*	1.8	*277*	29				
229	1.6	*232*	19	*274.5*	1.8	*277.5*	30				
229.5	1.6	*232.5*	19	*275*	1.8	*278*	28				
230	1.6	*233*	19	*275.5*	1.7	*278.5*	20				
230.5	1.6	*233.5*	20	*276*	1.7	*279*	19				

Table 8: Wet bulk density and magnetic susceptibility data of core GC 36

GC 36	*Depth* (cm)	Density (g/cm^3)	*Depth* (cm)	Mag Sus SI x 10^{-5}	*Depth* (cm)	Density (g/cm^3)	*Depth* (cm)	Mag Sus SI x 10^{-5}	*Depth* (cm)	Density (g/cm^3)	*Depth* (cm)	Mag Sus SI x 10^{-5}
	0.9	1.0	1	7	45.9	1.1	46	12	90.9	1.3	91	13
	1.4	1.1	1.5	11	46.4	1.1	46.5	12	91.4	1.3	91.5	12
	1.9	1.1	2	12	46.9	1.1	47	11	91.9	1.3	92	13
	2.4	1.1	2.5	15	47.4	1.1	47.5	11	92.4	1.3	92.5	13
	2.9	1.0	3	18	47.9	1.1	48	11	92.9	1.4	93	13
	3.4	0.9	3.5	23	48.4	1.1	48.5	12	93.4	1.4	93.5	13
	3.9	0.8	4	23	48.9	1.1	49	14	93.9	1.4	94	13
	4.4	0.6	4.5	14	49.4	1.1	49.5	11	94.4	1.4	94.5	12
	4.9	0.6	5	16	49.9	1.2	50	11	94.9	1.4	95	13
	5.4	0.8	5.5	19	50.4	1.2	50.5	11	95.4	1.4	95.5	13
	5.9	0.9	6	22	50.9	1.2	51	11	95.9	1.4	96	13
	6.4	1.0	6.5	22	51.4	1.3	51.5	12	96.4	1.4	96.5	13
	6.9	1.0	7	22	51.9	1.3	52	11	96.9	1.3	97	12
	7.4	1.0	7.5	22	52.4	1.3	52.5	11	97.4	1.3	102.86	12
	7.9	1.0	8	22	52.9	1.3	53	11	97.9	1.4	103.36	12
	8.4	1.1	8.5	21	53.4	1.3	53.5	11	98.4	1.4	103.86	13
	8.9	1.1	9	20	53.9	1.3	54	11	98.9	1.4	104.36	13
	9.4	1.1	9.5	20	54.4	1.3	54.5	11	99.4	1.4	104.86	12
	9.9	1.1	10	19	54.9	1.3	55	12	99.9	1.4	105.36	13
	10.4	1.1	10.5	19	55.4	1.3	55.5	11	100.4	1.4	105.86	13
	10.9	1.1	11	18	55.9	1.3	56	11	101.6	1.3	106.36	13
	11.4	1.1	11.5	18	56.4	1.2	56.5	11	102.1	1.4	106.86	13
	11.9	1.1	12	19	56.9	1.2	57	11	102.6	1.4	107.36	13
	12.4	1.1	12.5	19	57.4	1.3	57.5	11	103.1	1.4	107.86	13
	12.9	1.1	13	20	57.9	1.3	58	11	103.6	1.4	108.36	13
	13.4	1.1	13.5	21	58.4	1.3	58.5	11	104.1	1.4	108.86	13
	13.9	1.1	14	18	58.9	1.3	59	11	104.6	1.3	109.36	12
	14.4	1.1	14.5	18	59.4	1.3	59.5	11	105.1	1.3	109.86	11
	14.9	1.1	15	18	59.9	1.3	60	10	105.6	1.2	110.36	12
	15.4	1.1	15.5	18	60.4	1.3	60.5	11	106.1	1.2	110.86	13
	15.9	1.2	16	18	60.9	1.3	61	11	106.6	1.3	111.36	12
	16.4	1.2	16.5	18	61.4	1.3	61.5	11	107.1	1.3	111.86	13
	16.9	1.2	17	18	61.9	1.3	62	12	107.6	1.3	112.36	13
	17.4	1.2	17.5	17	62.4	1.3	62.5	12	108.1	1.3	112.86	13
	17.9	1.2	18	17	62.9	1.3	63	12	108.6	1.3	113.36	13
	18.4	1.2	18.5	17	63.4	1.3	63.5	13	109.1	1.3	113.86	13
	18.9	1.2	19	17	63.9	1.2	64	16	109.6	1.3	114.36	13
	19.4	1.2	19.5	17	64.4	1.2	64.5	16	110.1	1.3	114.86	12
	19.9	1.2	20	17	64.9	1.3	65	14	110.6	1.4	115.36	11
	20.4	1.2	20.5	16	65.4	1.3	65.5	15	111.1	1.4	115.86	12
	20.9	1.2	21	16	65.9	1.3	66	15	111.6	1.4	116.36	12
	21.4	1.2	21.5	16	66.4	1.3	66.5	13	112.1	1.4	116.86	12
	21.9	1.2	22	15	66.9	1.3	67	12	112.6	1.4	117.36	13
	22.4	1.2	22.5	15	67.4	1.3	67.5	11	113.1	1.3	117.86	12
	22.9	1.2	23	15	67.9	1.3	68	11	113.6	1.4	118.36	12
	23.4	1.2	23.5	15	68.4	1.3	68.5	11	114.1	1.4	118.86	12
	23.9	1.1	24	15	68.9	1.2	69	10	114.6	1.4	119.36	12
	24.4	1.2	24.5	16	69.4	1.3	69.5	10	115.1	1.4	119.86	11
	24.9	1.2	25	16	69.9	1.3	70	11	115.6	1.4	120.36	12
	25.4	1.2	25.5	16	70.4	1.2	70.5	11	116.1	1.4	120.86	12
	25.9	1.2	26	15	70.9	1.2	71	11	116.6	1.4	121.36	12
	26.4	1.2	26.5	15	71.4	1.2	71.5	11	117.1	1.4	121.86	12
	26.9	1.1	27	14	71.9	1.2	72	11	117.6	1.4	122.36	11
	27.4	1.1	27.5	14	72.4	1.3	72.5	11	118.1	1.4	122.86	11
	27.9	1.1	28	15	72.9	1.2	73	11	118.6	1.4	123.36	10
	28.4	1.2	28.5	15	73.4	1.3	73.5	12	119.1	1.4	123.86	10
	28.9	1.2	29	15	73.9	1.3	74	11	119.6	1.4	124.36	12
	29.4	1.2	29.5	15	74.4	1.3	74.5	12	120.1	1.4	124.86	13
	29.9	1.2	30	15	74.9	1.3	75	13	120.6	1.4	125.36	13
	30.4	1.2	30.5	15	75.4	1.3	75.5	12	121.1	1.4	125.86	13
	30.9	1.2	31	15	75.9	1.3	76	11	121.6	1.4	126.36	12
	31.4	1.2	31.5	15	76.4	1.3	76.5	12	122.1	1.4	126.86	12
	31.9	1.2	32	14	76.9	1.2	77	11	122.6	1.4	127.36	12
	32.4	1.2	32.5	14	77.4	1.3	77.5	11	123.1	1.4	127.86	12
	32.9	1.2	33	14	77.9	1.3	78	11	123.6	1.4	128.36	11
	33.4	1.2	33.5	14	78.4	1.3	78.5	11	124.1	1.4	128.86	11
	33.9	1.2	34	15	78.9	1.3	79	11	124.6	1.4	129.36	11
	34.4	1.2	34.5	15	79.4	1.3	79.5	11	125.1	1.4	129.86	11
	34.9	1.2	35	15	79.9	1.3	80	11	125.6	1.4	130.36	11
	35.4	1.2	35.5	17	80.4	1.3	80.5	12	126.1	1.4	130.86	11
	35.9	1.2	36	15	80.9	1.3	81	13	126.6	1.5	131.36	11
	36.4	1.2	36.5	13	81.4	1.3	81.5	13	127.1	1.4	131.86	11
	36.9	1.2	37	13	81.9	1.3	82	13	127.6	1.5	132.36	12
	37.4	1.2	37.5	13	82.4	1.3	82.5	13	128.1	1.5	132.86	12
	37.9	1.2	38	12	82.9	1.3	83	13	128.6	1.5	133.36	13
	38.4	1.2	38.5	12	83.4	1.3	83.5	13	129.1	1.5	133.86	12
	38.9	1.2	39	12	83.9	1.3	84	13	129.6	1.5	134.36	12
	39.4	1.2	39.5	12	84.4	1.3	84.5	13	130.1	1.5	134.86	12
	39.9	1.2	40	13	84.9	1.3	85	13	130.6	1.5	135.36	12
	40.4	1.2	40.5	12	85.4	1.3	85.5	13	131.1	1.5	135.86	12
	40.9	1.2	41	12	85.9	1.3	86	12	131.6	1.5	136.36	12
	41.4	1.1	41.5	12	86.4	1.3	86.5	8	132.1	1.5	136.86	12
	41.9	1.1	42	12	86.9	1.3	87	10	132.6	1.5	137.36	12
	42.4	1.1	42.5	11	87.4	1.3	87.5	12	133.1	1.5	137.86	12
	42.9	1.1	43	11	87.9	1.3	88	12	133.6	1.5	138.36	13
	43.4	1.1	43.5	12	88.4	1.3	88.5	12	134.1	1.5	138.86	13
	43.9	1.1	44	12	88.9	1.3	89	12	134.6	1.5	139.36	13
	44.4	1.1	44.5	12	89.4	1.3	89.5	13	135.1	1.5	139.86	13
	44.9	1.1	45	12	89.9	1.3	90	12	135.6	1.5	140.36	13
	45.4	1.2	45.5	12	90.4	1.3	90.5	13	136.1	1.5	140.86	13

Table 2 continued: Wet bulk density and magnetic susceptibility data of core GC 36

Depth (cm)	Density (g/cm^3)	*Depth (cm)*	Mag Sus SI x 10^{-5}	*Depth (cm)*	Density (g/cm^3)	*Depth (cm)*	Mag Sus SI x 10^{-5}	*Depth (cm)*	Density (g/cm^3)	*Depth (cm)*	Mag Sus SI x 10^{-5}
136.6	1.5	141.36	13	181.6	1.5	186.36	14	226.96	1.4	235.86	8
137.1	1.5	141.86	12	182.1	1.4	186.86	14	227.46	1.4	236.36	9
137.6	1.6	142.36	12	182.6	1.4	187.36	13	227.96	1.4	236.86	9
138.1	1.6	142.86	13	183.1	1.4	187.86	13	228.46	1.4	237.36	9
138.6	1.6	143.36	13	183.6	1.4	188.36	13	228.96	1.4	237.86	10
139.1	1.6	143.86	13	184.1	1.4	188.86	13	229.46	1.4	238.36	11
139.6	1.6	144.36	13	184.6	1.4	189.36	14	229.96	1.4	238.86	12
140.1	1.6	144.86	13	185.1	1.4	189.86	13	230.46	1.4	239.36	11
140.6	1.6	145.36	14	185.6	1.4	190.36	14	230.96	1.4	239.86	11
141.1	1.6	145.86	13	186.1	1.4	190.86	14	231.46	1.4	240.36	13
141.6	1.5	146.36	14	186.6	1.4	191.36	13	231.96	1.4	240.86	13
142.1	1.5	146.86	14	187.1	1.4	191.86	14	232.46	1.5	241.36	13
142.6	1.5	147.36	14	187.6	1.4	192.36	14	232.96	1.4	241.86	14
143.1	1.5	147.86	13	188.1	1.4	192.86	14	233.46	1.4	242.36	14
143.6	1.5	148.36	14	188.6	1.4	193.36	14	233.96	1.4	242.86	13
144.1	1.5	148.86	14	189.1	1.4	193.86	14	234.46	1.4	243.36	12
144.6	1.5	149.36	14	189.6	1.4	194.36	14	234.96	1.4	243.86	12
145.1	1.5	149.86	14	190.1	1.4	194.86	14	235.46	1.4	244.36	14
145.6	1.5	150.36	18	190.6	1.4	195.36	14	235.96	1.5	244.86	13
146.1	1.5	150.86	14	191.1	1.4	195.86	14	236.46	1.4	245.36	13
146.6	1.4	151.36	14	191.6	1.4	196.36	15	236.96	1.4	245.86	10
147.1	1.4	151.86	14	192.1	1.4	196.86	14	237.46	1.4	246.36	10
147.6	1.4	152.36	14	192.6	1.4	197.36	15	237.96	1.4	246.86	14
148.1	1.4	152.86	13	193.1	1.4	197.86	14	238.46	1.4	247.36	14
148.6	1.4	153.36	13	193.6	1.4	198.36	14	238.96	1.5	247.86	14
149.1	1.4	153.86	14	194.1	1.4	198.86	15	239.46	1.5	248.36	13
149.6	1.4	154.36	13	194.6	1.4	199.36	15	239.96	1.5	248.86	14
150.1	1.4	154.86	13	195.1	1.4	199.86	14	240.46	1.5	249.36	14
150.6	1.4	155.36	14	195.6	1.4	200.36	14	240.96	1.5	249.86	14
151.1	1.4	155.86	14	196.1	1.4	200.86	13	241.46	1.5	250.36	14
151.6	1.4	156.36	14	196.6	1.4	201.36	12	241.96	1.5	250.86	13
152.1	1.4	156.86	13	197.1	1.4	201.86	12	242.46	1.5	251.36	13
152.6	1.4	157.36	13	197.6	1.4	206.86	6	242.96	1.5	251.86	13
153.1	1.4	157.86	13	198.1	1.5	207.36	6	243.46	1.5	252.36	13
153.6	1.4	158.36	13	198.6	1.5	207.86	6	243.96	1.5	252.86	13
154.1	1.4	158.86	14	199.1	1.4	208.36	6	244.46	1.5	253.36	14
154.6	1.4	159.36	14	199.6	1.5	208.86	7	244.96	1.5	253.86	13
155.1	1.4	159.86	13	200.1	1.4	209.36	7	245.46	1.5	254.36	15
155.6	1.4	160.36	13	200.6	1.4	209.86	7	245.96	1.5	254.86	14
156.1	1.4	160.86	14	201.1	1.5	210.36	7	246.46	1.5	255.36	15
156.6	1.4	161.36	13	201.6	1.4	210.86	7	246.96	1.5	255.86	14
157.1	1.4	161.86	13	202.1	1.4	211.36	7	247.46	1.5	256.36	14
157.6	1.4	162.36	13	202.96	1.3	211.86	7	247.96	1.5	256.86	14
158.1	1.4	162.86	14	203.46	1.4	212.36	7	248.46	1.5	257.36	14
158.6	1.4	163.36	13	203.96	1.4	212.86	7	248.96	1.5	257.86	13
159.1	1.4	163.86	14	204.46	1.4	213.36	7	249.46	1.5	258.36	13
159.6	1.4	164.36	13	204.96	1.4	213.86	7	249.96	1.5	258.86	13
160.1	1.4	164.86	14	205.46	1.4	214.36	7	250.46	1.5	259.36	13
160.6	1.4	165.36	14	205.96	1.4	214.86	7	250.96	1.5	259.86	13
161.1	1.5	165.86	14	206.46	1.4	215.36	7	251.46	1.5	260.36	13
161.6	1.5	166.36	14	206.96	1.4	215.86	7	251.96	1.5	260.86	13
162.1	1.5	166.86	14	207.46	1.4	216.36	7	252.46	1.5	261.36	14
162.6	1.5	167.36	14	207.96	1.4	216.86	7	252.96	1.5	261.86	14
163.1	1.5	167.86	14	208.46	1.4	217.36	8	253.46	1.5	262.36	14
163.6	1.5	168.36	13	208.96	1.4	217.86	8	253.96	1.5	262.86	14
164.1	1.5	168.86	14	209.46	1.4	218.36	7	254.46	1.5	263.36	13
164.6	1.5	169.36	14	209.96	1.4	218.86	7	254.96	1.5	263.86	14
165.1	1.5	169.86	13	210.46	1.4	219.36	8	255.46	1.5	264.36	14
165.6	1.5	170.36	14	210.96	1.4	219.86	8	255.96	1.5	264.86	14
166.1	1.5	170.86	14	211.46	1.4	220.36	8	256.46	1.5	265.36	14
166.6	1.5	171.36	14	211.96	1.4	220.86	9	256.96	1.5	265.86	14
167.1	1.5	171.86	14	212.46	1.4	221.36	9	257.46	1.5	266.36	13
167.6	1.5	172.36	14	212.96	1.4	221.86	9	257.96	1.5	266.86	14
168.1	1.5	172.86	14	213.46	1.4	222.36	9	258.46	1.5	267.36	13
168.6	1.5	173.36	14	213.96	1.4	222.86	9	258.96	1.5	267.86	14
169.1	1.5	173.86	14	214.46	1.4	223.36	9	259.46	1.5	268.36	14
169.6	1.5	174.36	13	214.96	1.4	223.86	8	259.96	1.5	268.86	13
170.1	1.4	174.86	13	215.46	1.4	224.36	5	260.46	1.5	269.36	13
170.6	1.5	175.36	14	215.96	1.4	224.86	6	260.96	1.5	269.86	14
171.1	1.5	175.86	14	216.46	1.4	225.36	8	261.46	1.5	270.36	13
171.6	1.5	176.36	14	216.96	1.4	225.86	9	261.96	1.5	270.86	14
172.1	1.5	176.86	14	217.46	1.4	226.36	9	262.46	1.5	271.36	14
172.6	1.5	177.36	14	217.96	1.4	226.86	9	262.96	1.5	271.86	14
173.1	1.5	177.86	14	218.46	1.4	227.36	9	263.46	1.5	272.36	14
173.6	1.5	178.36	14	218.96	1.4	227.86	9	263.96	1.5	272.86	13
174.1	1.4	178.86	14	219.46	1.4	228.36	9	264.46	1.5	273.36	13
174.6	1.4	179.36	14	219.96	1.4	228.86	10	264.96	1.5	273.86	12
175.1	1.5	179.86	14	220.46	1.4	229.36	10	265.46	1.5	274.36	13
175.6	1.4	180.36	14	220.96	1.4	229.86	11	265.96	1.5	274.86	13
176.1	1.5	180.86	14	221.46	1.4	230.36	11	266.46	1.5	275.36	13
176.6	1.5	181.36	13	221.96	1.4	230.86	11	266.96	1.5	275.86	13
177.1	1.5	181.86	14	222.46	1.4	231.36	10	267.46	1.5	276.36	13
177.6	1.5	182.36	13	222.96	1.4	231.86	10	267.96	1.5	276.86	13
178.1	1.5	182.86	14	223.46	1.4	232.36	9	268.46	1.4	277.36	13
178.6	1.5	183.36	14	223.96	1.4	232.86	8	268.96	1.4	277.86	13
179.1	1.5	183.86	14	224.46	1.4	233.36	8	269.46	1.5	278.36	13
179.6	1.5	184.36	14	224.96	1.4	233.86	9	269.96	1.5	278.86	13
180.1	1.4	184.86	14	225.46	1.4	234.36	8	270.46	1.5	279.36	13
180.6	1.5	185.36	14	225.96	1.4	234.86	7	270.96	1.5	279.86	12
181.1	1.4	185.86	14	226.46	1.4	235.36	8	271.46	1.5	280.36	13

Table 2 continued: Wet bulk density and magnetic susceptibility data of core GC 36

Depth (cm)	Density (g/cm^3)	*Depth (cm)*	Mag Sus SI x 10^{-5}	*Depth (cm)*	Density (g/cm^3)	*Depth (cm)*	Mag Sus SI x 10^{-5}	*Depth (cm)*	Density (g/cm^3)	*Depth (cm)*	Mag Sus SI x 10^{-5}
271.96	1.5	280.86	12	318.16	1.5	328.36	13	363.16	1.5	373.36	8
272.46	1.5	281.36	12	318.66	1.5	328.86	13	363.66	1.5	373.86	11
272.96	1.5	281.86	12	319.16	1.5	329.36	13	364.16	1.5	374.36	13
273.46	1.5	282.36	13	319.66	1.5	329.86	13	364.66	1.5	374.86	13
273.96	1.5	282.86	13	320.16	1.5	330.36	13	365.16	1.5	375.36	13
274.46	1.5	283.36	12	320.66	1.5	330.86	13	365.66	1.5	375.86	13
274.96	1.5	283.86	12	321.16	1.5	331.36	12	366.16	1.5	376.36	13
275.46	1.5	284.36	12	321.66	1.5	331.86	12	366.66	1.5	376.86	14
275.96	1.5	284.86	13	322.16	1.5	332.36	12	367.16	1.5	377.36	13
276.46	1.5	285.36	13	322.66	1.5	332.86	12	367.66	1.5	377.86	13
276.96	1.5	285.86	12	323.16	1.5	333.36	12	368.16	1.5	378.36	13
277.46	1.4	286.36	13	323.66	1.5	333.86	12	368.66	1.5	378.86	13
277.96	1.5	286.86	13	324.16	1.5	334.36	12	369.16	1.5	379.36	14
278.46	1.4	287.36	13	324.66	1.5	334.86	12	369.66	1.5	379.86	13
278.96	1.5	287.86	13	325.16	1.5	335.36	12	370.16	1.5	380.36	14
279.46	1.5	288.36	13	325.66	1.5	335.86	11	370.66	1.5	380.86	15
279.96	1.5	288.86	13	326.16	1.5	336.36	11	371.16	1.5	381.36	15
280.46	1.5	289.36	12	326.66	1.5	336.86	11	371.66	1.5	381.86	14
280.96	1.5	289.86	12	327.16	1.5	337.36	11	372.16	1.5	382.36	13
281.46	1.5	290.36	13	327.66	1.5	337.86	11	372.66	1.4	382.86	13
281.96	1.5	290.86	13	328.16	1.5	338.36	11	373.16	1.5	383.36	13
282.46	1.5	291.36	13	328.66	1.5	338.86	10	373.66	1.5	383.86	12
282.96	1.5	291.86	13	329.16	1.5	339.36	10	374.16	1.5	384.36	12
283.46	1.5	292.36	13	329.66	1.5	339.86	10	374.66	1.5	384.86	13
283.96	1.5	292.86	13	330.16	1.5	340.36	10	375.16	1.5	385.36	14
284.46	1.5	293.36	13	330.66	1.5	340.86	10	375.66	1.5	385.86	14
284.96	1.5	293.86	12	331.16	1.5	341.36	12	376.16	1.5	386.36	11
285.46	1.4	294.36	12	331.66	1.5	341.86	13	376.66	1.5	386.86	7
285.96	1.5	294.86	12	332.16	1.5	342.36	12	377.16	1.5	387.36	8
286.46	1.5	295.36	13	332.66	1.5	342.86	12	377.66	1.5	387.86	8
286.96	1.5	295.86	12	333.16	1.5	343.36	13	378.16	1.5	388.36	11
287.46	1.4	296.36	12	333.66	1.5	343.86	13	378.66	1.5	388.86	13
287.96	1.5	296.86	12	334.16	1.5	344.36	13	379.16	1.5	389.36	11
288.46	1.4	297.36	12	334.66	1.5	344.86	13	379.66	1.5		
288.96	1.5	297.86	12	335.16	1.5	345.36	13	380.16	1.5		
289.46	1.5	298.36	13	335.66	1.5	345.86	13	380.66	1.5		
289.96	1.4	298.86	13	336.16	1.5	346.36	13	381.16	1.5		
290.46	1.5	299.36	13	336.66	1.5	346.86	12	381.66	1.5		
290.96	1.5	299.86	11	337.16	1.5	347.36	12	382.16	1.5		
291.46	1.4	300.36	13	337.66	1.5	347.86	12	382.66	1.5		
291.96	1.4	300.86	12	338.16	1.5	348.36	12	383.16	1.5		
292.46	1.4	301.36	13	338.66	1.5	348.86	12	383.66	1.5		
292.96	1.4	301.86	13	339.16	1.5	349.36	12	384.16	1.5		
293.46	1.4	302.36	13	339.66	1.5	349.86	14	384.66	1.5		
293.96	1.4	305.36	12	340.16	1.5	350.36	14	385.16	1.5		
294.46	1.4	305.86	12	340.66	1.5	350.86	13	385.66	1.5		
294.96	1.5	306.36	12	341.16	1.5	351.36	13	386.16	1.5		
295.46	1.4	306.86	12	341.66	1.5	351.86	12	386.66	1.5		
295.96	1.4	307.36	12	342.16	1.5	352.36	13	387.16	1.5		
296.46	1.5	307.86	11	342.66	1.5	352.86	13	387.66	1.4		
296.96	1.4	308.36	10	343.16	1.5	353.36	13	388.16	1.5		
297.46	1.5	308.86	11	343.66	1.5	353.86	13	388.66	1.5		
297.96	1.5	309.36	12	344.16	1.5	354.36	13	389.16	1.4		
298.46	1.5	309.86	12	344.66	1.5	354.86	13	389.66	1.3		
298.96	1.5	310.36	13	345.16	1.5	355.36	13				
299.46	1.5	310.86	13	345.66	1.5	355.86	13				
299.96	1.5	311.36	12	346.16	1.5	356.36	13				
300.46	1.5	311.86	13	346.66	1.5	356.86	13				
300.96	1.5	312.36	14	347.16	1.5	357.36	13				
301.46	1.4	312.86	13	347.66	1.5	357.86	15				
301.96	1.5	313.36	13	348.16	1.5	358.36	13				
302.46	1.5	313.86	13	348.66	1.5	358.86	13				
302.96	1.5	314.36	13	349.16	1.5	359.36	13				
304.66	1.4	314.86	13	349.66	1.5	359.86	13				
305.16	1.5	315.36	13	350.16	1.5	360.36	13				
305.66	1.5	315.86	14	350.66	1.5	360.86	13				
306.16	1.5	316.36	14	351.16	1.5	361.36	13				
306.66	1.4	316.86	13	351.66	1.5	361.86	13				
307.16	1.3	317.36	13	352.16	1.5	362.36	13				
307.66	1.4	317.86	13	352.66	1.5	362.86	13				
308.16	1.4	318.36	13	353.16	1.5	363.36	13				
308.66	1.5	318.86	13	353.66	1.5	363.86	13				
309.16	1.5	319.36	13	354.16	1.5	364.36	13				
309.66	1.5	319.86	13	354.66	1.5	364.86	13				
310.16	1.4	320.36	13	355.16	1.5	365.36	13				
310.66	1.4	320.86	13	355.66	1.5	365.86	13				
311.16	1.4	321.36	13	356.16	1.5	366.36	12				
311.66	1.5	321.86	13	356.66	1.5	366.86	12				
312.16	1.5	322.36	13	357.16	1.4	367.36	13				
312.66	1.5	322.86	13	357.66	1.4	367.86	13				
313.16	1.5	323.36	13	358.16	1.5	368.36	12				
313.66	1.5	323.86	13	358.66	1.5	368.86	12				
314.16	1.5	324.36	13	359.16	1.5	369.36	12				
314.66	1.5	324.86	13	359.66	1.5	369.86	12				
315.16	1.5	325.36	13	360.16	1.5	370.36	13				
315.66	1.5	325.86	13	360.66	1.5	370.86	12				
316.16	1.5	326.36	13	361.16	1.5	371.36	12				
316.66	1.5	326.86	13	361.66	1.5	371.86	9				
317.16	1.5	327.36	13	362.16	1.5	372.36	4				
317.66	1.5	327.86	13	362.66	1.5	372.86	4				

Table 9: Grain size data of GC 51

GC 51	Clay	Silt	Silt	Very fine sand	Fine sand	Medium sand	Coarse sand	Very coarse sand	Granule	Pebble
	<2 µm	2-63 µm	and	63-125 µm	125-250 µm	250-500 µm	500-1000 µm	1-2mm	2-4mm	>4mm
Depth (cm)	%	%	clay	%	%	%	%			
1	1.85	6.92	8.77	8.63	31.3	27.9	8.9	3.6	4	6.9
5.5	3.07	26.63	29.7	25.9	36.7	7.6	0.1			
11	3.5	31.3	34.8	23.2	35.6	6.3	0.1			
15.5	3.8	33.3	37.1	27.5	31.8	3.58	0.02			
21	4.46	42.04	46.5	22.1	26.7	4.68	0.02			
26	10.2	34.7	44.9	17.6	28.4	4.4		1.4	2	1.3
31	2.92	26.08	29	32.9	35.3	2.78	0.02			
36	2.65	22.95	25.6	28.8	41.7	3.8	0.1			
38.5	3.95	35.85	39.8	28.2	29.8	2.18	0.02			
46	5.05	49.55	54.6	25.8	17.7	1.8	0.1			
51	5.93	54.97	60.9	24.5	12.9	1.68	0.02			
56	6.75	63.85	70.6	19.9	9.46	0.04				
61	6.9	64.3	71.2	20.1	8.68	0.02				
65.5	5.28	47.22	52.5	26.3	20.9	0.3				
74	6.23	58.37	64.6	24.4	10.98	0.02				
79	8.25	66.85	75.1	17.2	7.2	0.5				
90	7.34	68.06	75.4	18.2	6.2	0.2				
93.5	6.72	64.08	70.8	21.4	7.78	0.02				
97.5	6.69	65.71	72.4	20	7.58	0.02				
102.5	8.42	75.68	84.1	11.9	3.8	0.2				
107.5	7.75	71.85	79.6	16.8	3.599	0.001				
112	8.15	71.45	79.6	16.4	3.8	0.2				
117.5	7.5	62.6	70.1	14.4	13.3	1.8	0.4			
122.5	7.19	62.31	69.5	22.8	7.68	0.02				
127.5	9.12	75.78	84.9	11	3.1	1				
132.5	5.73	54.87	60.6	29.3	10.07	0.03				
135	6.52	56.48	63	25.2	11.76	0.04				
142.5	8.46	70.24	78.7	16.6	4.6	0.1				
147.5	10.4	80.7	91.1	7.1	1.8					
152.5	10	77.8	87.8	9	2.9	0.3				
157.5	8.87	75.03	83.9	12.9	3.16	0.04				
162.5	9.3	72.9	82.2	13.6	4.1	0.1				
167.5	11.3	81.1	92.4	6.5	1.1					
172.5	10.5	79.9	90.4	8.2	1.4					
177.5	10.1	78.7	88.8	8.8	2.1	0.3				
187	12	81.7	93.7	5.2	1.06	0.04				
191	13.3	80.9	94.2	5	0.8					
199	12.1	81.7	93.8	5.6	0.6					
203.5	14.8	80.5	95.3	3.7	1					
211	12.6	79.3	91.9	5.9	2.1	0.1				
214	12.6	79	91.6	6.2	2.19	0.01				
218.5	12.2	78.6	90.8	7.1	2.09	0.01				
223.5	13.9	79.2	93.1	5.3	1.6					
228.5	12.7	77.3	90	7.2	2.6	0.2				
238.5	17.1	79.1	96.2	2.9	0.9					
243.5	15.4	79.6	95	3.8	1.2					
248.5	15	79.3	94.3	4.5	1.19	0.01				
253.5	15.2	80.4	95.6	3.1	1.3					
258.5	15.5	81.4	96.9	2.1	0.98	0.02				
263.5	14.9	79.7	94.6	3.8	1.56	0.04				
268.5	13.2	80.3	93.5	4.2	2.1	0.2				
273.5	9.44	74.56	84	9	4.2	2.8				
276	13.5	79.2	92.7	4.3	2.5	0.5				
282.5	18.1	78.5	96.6	2.4	1					
290.5	18.2	80.6	98.8	1.2	0					
295.5	10.2	75.8	86	8.5	5.2	0.3				
298.5	6.27	68.83	75.1	17.4	4.2	2.4	0.9			
303	7.08	60.12	67.2	14.6	8.7	6.7	2.8			
308	7.05	60.55	67.6	13.4	8.3	7.4	3.3			

Table 10: Grain size data of GC 36

GC 36	Clay	Silt	Very fine sand	Fine sand	Medium sand
	<2 µm	2-63 µm	63-125 µm	125-250 µm	250-500 µm
Depth (cm)	%	%	%	%	%
7	3.78	91.62	3.8	0.799	0.001
11.5	3.94	91.16	4.3	0.6	
16	3.92	91.38	4.2	0.5	
21.5	4.53	90.47	4.5	0.5	
26	4.24	90.26	4.7	0.8	
31	3.75	90.85	4.9	0.5	
37	4.34	89.36	5.3	1	
46	3.58	90.62	5.3	0.5	
51.5	3.52	91.08	4.9	0.5	
56	3.84	89.76	4.8	1.4	0.2
61.5	4.14	88.36	5.8	1.68	0.02
66	3.65	89.65	5.2	1.49	0.01
71.5	4.02	88.88	5.4	1.699	0.001
77	4.11	88.59	4.8	1.9	0.6
86	4.34	89.86	4.4	1.3	0.1
91	4.29	88.01	4.7	2.2	0.8
96	4.28	88.62	5	1.7	0.4
107	4.11	90.69	4.4	0.8	
112	4.7	89.4	4.9	0.9	0.1
117	4.35	90.35	4.5	0.8	
122.5	4.27	89.63	4.9	1.19	0.01
127	4.48	88.22	5.9	1.399	0.001
132	4.17	84.43	8.6	2.79	0.01
137	3.3	77.1	15.2	4.39	0.01
139.5	3.56	77.24	14.3	4.88	0.02
147	4.88	89.52	4.8	0.8	
152.5	4.99	89.41	4.7	0.899	0.001
157.5	5	89.8	5	0.2	
162	4.81	89.09	4.5	1.3	0.3
167	4.63	89.47	5.4	0.5	
172	4.84	89.46	5.1	0.6	
177.5	4.96	88.34	5	1.69	0.01
180	4.85	88.85	4.9	1.4	
187	4.79	89.61	4.7	0.9	
194	4.82	90.48	4.3	0.4	
201	4.55	89.75	4.7	0.99	0.01
208.36	4.96	89.14	4.6	1.28	0.02
212.86	4.75	89.65	4.4	1.17	0.03
217.86	4.87	89.93	4.6	0.6	
222.86	4.93	89.77	4.3	1	
227.86	4.53	90.97	3.9	0.6	
233.36	4.84	90.96	4.199	0.001	
237.86	4.31	88.19	5.2	2.1	0.2
242.86	4.77	88.33	5.2	1.6	0.1
247.86	4.44	89.96	5	0.6	
253.36	4.6	88.8	5.1	1.4	0.1
257.86	4.84	88.56	5.3	1.299	0.001
263.36	4.67	89.53	5.3	0.5	
267.86	4.75	88.25	5.1	1.88	0.02
272.86	4.93	91.17	3.8	0.1	
277.86	4.78	89.32	4.9	1	
282.86	4.52	89.48	4.5	1.3	0.2
287.86	4.72	89.28	5.2	0.799	0.001
292.86	4.5	89.5	5.1	0.9	
297.36	4.56	89.44	5.2	0.8	
304.86	4.52	89.98	4.9	0.6	
309.86	4.71	90.39	4.3	0.6	
314.86	4.88	89.62	4.7	0.8	
319.86	4.74	89.16	4.7	1.3	0.1
324.86	4.79	88.81	5.2	1.197	0.003
329.86	4.76	89.24	4.8	1.1	0.1
334.36	4.43	89.47	5	1.09	0.01
339.36	4.37	90.73	4.5	0.4	
344.86	4.54	88.76	4.8	1.86	0.04
349.86	4.78	88.92	4.7	1.5	0.1
354.86	4.83	88.37	4.8	1.5	0.5
359.86	4.79	89.41	4.5	1.2	0.1
364.86	4.94	89.06	4.5	0.9	0.6
369.86	4.88	87.52	4.9	1.7	1
374.86	4.93	89.97	4.4	0.7	
379.36	4.51	90.79	4.3	0.4	
384.36	4.51	90.49	4.4	0.6	

Table 11: Results of C_{org}, $CaCO_3$, N_{tot}, C/N and $\delta^{13}C$-C_{org} analyses of core GC 51 and GC 36

Core	Depth (cm)	Corg (%)	$CaCO_3$ (%)	N_{tot} (%)	C/N	$\delta^{13}C$-C_{org} (V-PDB)
GC 36	5	2.9	14.2	0.41	8.1	-21.5
	10	2.6	14.3	0.39	7.8	-21.2
	15	2.58	14.7	0.38	8.0	-21.1
	20	2.51	15.2	0.37	7.9	-21.1
	25	2.54	15.2	0.39	7.6	-21.1
	30	2.47	15.2	0.38	7.7	-21.0
	35	2.44	17.0	0.37	7.8	-21.3
	40	2.42	16.5	0.37	7.6	-20.9
	45	2.52	18.4	0.37	8.0	-21.0
	50	2.51	17.3	0.38	7.8	-20.9
	55	2.5	17.4	0.37	7.8	-21.0
	60	2.54	17.5	0.38	7.8	-20.9
	65	2.6	20.2	0.38	8.0	-21.0
	70	2.59	19.0	0.37	8.1	-21.0
	75	2.46	18.9	0.37	7.7	-21.0
	80	2.4	18.6	0.36	7.8	-21.0
	85	2.38	17.9	0.34	8.1	-21.0
	90	2.33	17.7	0.35	7.8	-20.9
	95	2.45	18.6	0.38	7.5	-21.0
	99	2.43	18.4	0.38	7.4	-21.0
	106	2.43	17.5	0.37	7.7	-20.9
	111	2.37	18.0	0.37	7.4	-20.9
	116	2.29	17.5	0.36	7.5	-20.9
	121	2.23	17.6	0.35	7.5	-20.9
	126	2.06	17.2	0.32	7.5	-20.8
	131	1.9	18.0	0.30	7.3	-20.8
	136	1.91	17.4	0.27	8.1	-21.0
	141	1.43	15.7	0.21	8.1	-20.9
	146	1.87	16.7	0.30	7.2	-21.0
	151	2.32	19.5	0.35	7.7	-20.9
	156	2.28	19.7	0.35	7.6	-20.9
	161	2.16	18.6	0.33	7.5	-20.9
	166	2.11	18.7	0.34	7.3	-20.9
	171	2.13	18.4	0.33	7.5	-20.9
	176	2.15	18.3	0.34	7.4	-21.0
	181	2.19	18.5	0.35	7.3	-21.0
	186	2.18	18.7	0.34	7.4	-21.0
	191	2.25	18.0	0.35	7.6	-21.0
	196	2.18	18.5	0.34	7.4	-21.0
	200	2.21	18.1	0.35	7.4	-21.0
	207.36	2.25	18.4	0.35	7.6	-21.0
	212.36	2.14	17.9	0.33	7.6	-20.9
	217.36	2.24	18.5	0.34	7.7	-20.8
	222.36	2.25	18.8	0.34	7.7	-20.9
	227.36	2.27	19.2	0.35	7.7	-20.9
	232.36	2.28	19.4	0.35	7.7	-21.0
	237.36	2.17	18.7	0.33	7.8	-21.0
	242.36	2.16	18.9	0.33	7.7	-21.1
	247.36	2.11	18.0	0.31	8.0	-21.1
	252.36	2.12	17.7	0.32	7.6	-21.1
	257.36	2.12	18.2	0.33	7.6	-21.1
	262.36	2.07	18.2	0.32	7.6	-21.1
	267.36	2.06	17.9	0.31	7.7	-21.2
	272.36	2.07	17.8	0.32	7.5	-21.1
	277.36	2	17.6	0.31	7.4	-21.0
	282.36	2.09	18.2	0.31	7.8	-21.0
	287.36	2.11	18.2	0.33	7.6	-21.1
	292.36	2.1	18.4	0.32	7.5	-21.0
	297.36	2.1	18.3	0.32	7.8	-21.0
	301.36	2.04	17.9	0.31	7.6	-21.0
	308.86	2.06	17.5	0.32	7.6	-21.2
	313.86	2.04	17.7	0.31	7.6	-21.1
	318.86	2	17.7	0.31	7.6	-21.1
	323.86	1.96	17.3	0.30	7.5	-21.1
	328.86	2.01	17.8	0.30	7.7	-21.2
	333.86	2.09	18.2	0.32	7.7	-21.2
	338.86	2.03	18.0	0.31	7.7	-21.3
	343.86	2.04	18.7	0.30	7.8	-21.2
	348.86	2.06	18.4	0.31	7.7	-21.2
	353.86	2.03	18.7	0.30	7.9	-21.2
	358.86	2.01	18.6	0.31	7.6	-21.2
	363.86	2.01	20.7	0.30	7.8	-21.2
	368.86	1.92	19.1	0.29	7.7	-21.1
	373.86	1.88	19.0	0.29	7.6	-21.3
	378.86	1.85	18.4	0.27	7.9	-21.3
	383.86	1.81	18.0	0.27	7.7	-21.4
	Average	***2.2***	***17.9***	***0.3***	***7.7***	***-21.0***

Core	Depth (cm)	Corg (%)	$CaCO_3$ (%)	N_{tot} (%)	C/N	$\delta^{13}C$-C_{org} (V-PDB)
GC 51	5	0.2	3.6	0.03	8.7	-24.6
	10	0.3	2.7	0.03	13.6	-24.8
	15	0.3	2.8	0.03	10.8	-25.1
	20	0.2	12.6	0.02	12.1	-25.4
	25	0.3	15.6	0.03	11.4	-25.5
	30	0.3	2.8	0.03	11.9	-25.3
	35	0.2	2.9	0.02	11.9	-26.2
	40	0.4	3.5	0.04	11.4	-25.9
	45	0.5	3.8	0.04	14.1	-26.2
	50	0.5	2.7	0.05	12.8	-25.2
	55	0.5	3.0	0.05	12.6	-25.0
	60	0.6	3.1	0.05	13.3	-24.9
	65	0.5	2.6	0.04	14.5	-25.3
	70	0.7	5.6	0.05	15.6	-25.3
	75	0.7	2.7	0.05	14.6	-24.9
	80	0.5	5.4	0.04	13.4	-25.2
	85	0.6	3.9	0.05	14.3	-25.4
	89	0.8	2.8	0.06	14.1	-25.2
	92	0.6	3.5	0.05	15.0	-25.1
	96	0.6	3.1	0.05	12.7	-24.9
	101	0.7	2.9	0.05	14.1	-24.8
	106	0.7	3.0	0.05	15.1	-24.7
	111	0.7	4.2	0.06	13.9	-24.8
	116	0.7	3.5	0.06	13.8	-24.7
	121	0.6	2.6	0.05	13.9	-24.7
	126	0.8	2.9	0.06	14.0	-24.6
	131	0.6	2.7	0.05	13.5	-24.7
	136	0.7	3.3	0.06	14.6	-24.8
	141	0.8	3.3	0.07	12.7	-24.7
	146	0.7	2.7	0.05	15.4	-24.7
	151	1.0	3.1	0.09	12.3	-24.6
	156	0.7	3.2	0.06	12.9	-24.6
	161	0.9	2.3	0.07	15.3	-24.6
	166	1.0	3.0	0.08	14.6	-24.7
	171	0.7	3.0	0.05	15.2	-24.6
	176	0.8	3.0	0.07	14.3	-24.7
	181	1.0	3.6	0.08	13.4	-24.5
	186	1.2	3.2	0.10	14.4	-24.7
	190	1.1	3.4	0.09	13.8	-24.9
	197.5	1.2	3.2	0.10	14.5	-24.5
	202.5	1.2	4.0	0.08	17.7	-24.4
	207.5	1.0	2.8	0.07	16.8	-24.3
	212.5	1.0	2.2	0.08	13.9	-24.2
	217.5	0.9	2.8	0.07	14.5	-24.2
	222.5	1.0	2.3	0.09	13.7	-24.4
	227.5	1.0	2.2	0.07	17.1	-24.4
	232.5	1.1	1.2	0.08	15.6	-24.5
	237.5	1.1	4.1	0.09	14.2	-24.7
	242.5	1.1	2.4	0.09	14.8	-24.4
	247.5	1.1	4.2	0.09	14.8	-24.4
	252.5	1.0	1.7	0.10	11.7	-24.5
	257.5	1.0	1.3	0.08	15.3	-24.6
	262.5	1.0	2.5	0.09	13.7	-24.6
	267.5	1.0	2.7	0.08	15.7	-24.6
	272.5	0.9	3.3	0.06	18.0	-24.7
	277.5	1.3	3.7	0.08	19.3	-24.4
	282.5	1.9	1.2	0.08	26.0	-23.8
	287.5	1.7	7.6	0.06	31.4	-23.9
	292.5	1.5	3.9	0.09	18.9	-24.3
	297.5	0.6	3.0	0.04	19.8	-24.9
	302.5	0.6	3.3	0.04	17.7	-25.4
	307.5	0.7	3.8	0.05	16.2	-25.5
	Average	***0.8***	***3.5***	***0.1***	***14.8***	***-24.8***